Visualizing the metazoan proliferation-differentiation decision *in vivo*

Abraham Q. Kohrman,[1#] Rebecca C. Adikes,[1#] Jayson J. Smith,[1] Michael A. Q. Martinez,[1] Taylor N. Medwig-Kinney,[1] Nicholas J. Palmisano, [1] Maria D. Sallee,[2] Ononnah B. Ahmed,[1] Nicholas Weeks,[1] Nuri Kim,[1] Simeiyun Liu,[1,3] Wan Zhang,[1] Ariel M. Pani[4] and David Q. Matus[1,5,*]

[1]Department of Biochemistry and Cell Biology, Stony Brook University, Stony Brook, NY 11794-5215, USA

[2]Department of Biology, Stanford University, Stanford, CA 94305, USA.

[3]Current address: Molecular, Cell and Developmental Biology, University of California Santa Cruz, Santa Cruz, CA 95064, USA

[4]Department of Biology, University of Virginia, Charlottesville, VA 22903, USA.

[5]Lead Contact

[#]These authors contributed equally to this work

*Correspondence: david.matus@stonybrook.edu

SUMMARY

During organismal development, differential regulation of the cell cycle is critical to many cell biological processes, including cell fate specification and differentiation. While the mechanisms of cell cycle regulation are well studied, how control of the cell cycle is linked to differentiated cellular behavior remains poorly understood, mostly due to our inability to directly and precisely measure cell cycle state. In order to characterize cell cycle state live, we adapted a cyclin-dependent kinase (CDK) biosensor for *in vivo* use in the roundworm nematode, *Caenorhabditis elegans*. The CDK biosensor measures the cytoplasmic-to-nuclear localization of a portion of human DNA Helicase B (DHB) fused to a fluorescent protein to assess cell cycle state. The dynamic localization of DHB results from phosphorylation of the biosensor by CDKs, thereby allowing for quantitative assessment of cell cycle state. We demonstrate here the use of this biosensor to quantify lineage-specific differences between cycling cells and to examine the proliferation-differentiation decision. Unlike other live cell imaging tools (e.g., FUCCI), we show that DHB can be used to distinguish between actively cycling cells in the G_1 phase of the cell cycle and terminally differentiated cells exited in G_0. Thus, we provide here a new resource to study the control and timing of the metazoan cell cycle during cell fate specification and differentiation.

KEYWORDS

Cell cycle, proliferation, differentiation, CDK biosensor, *C. elegans*, DNA Helicase B, G_0/G_1

INTRODUCTION

Throughout organismal development, individual cells must integrate intrinsic and extrinsic cues to give rise to a correctly patterned body plan. Decades of research in a variety of organisms has provided insight into links between cell cycle regulation and developmental events (Bouldin et al., 2014; Foe, 1989; Grosshans and Wieschaus, 2000; Matus et al., 2014; Matus et al., 2015; Murakami et al., 2004; Ogura et al., 2011). In metazoan embryos, the earliest cell divisions are characterized by rapid cleavage programs that alternate between DNA synthesis (S phase) and mitosis (M phase) (Elinson, 2011; Farrell and O'Farrell, 2014; Jukam et al., 2017; Langley et al., 2014; Wong et al., 2016). Later, tight cell cycle regulation is subsequently required to pattern germ layers (Elinson, 2011; Farrell and O'Farrell, 2014; Haeckel, 1903; Wong et al., 2016), which is often accompanied by morphogenesis (Bouldin and Kimelman, 2014a; Bouldin et al., 2014; Grosshans and Wieschaus, 2000; Hertzler and Clark, 1992; Kurth, 2005; Lahl et al., 2003; Matus et al., 2014; Matus et al., 2015; Murakami et al., 2004; Ogura et al., 2011). In some cases, the earliest morphogenetic events are intrinsically tied to the onset of the gap phases during interphase (G_1 and/or G_2) (Du et al., 2015; Edgar and McGhee, 1988; Foe, 1989; Mac Auley et al., 1993). Finally, cells in discrete lineages undergo terminal differentiation, exiting the cell cycle in a G_0 arrested state (Buttitta and Edgar, 2007; Buttitta et al., 2010; Buttitta et al., 2007; Clayton et al., 2008; Korzelius et al., 2011; Ma et al., 2019; Ruijtenberg and van den Heuvel, 2015; Saito et al., 2004; Singh et al., 2013; Singh et al., 2015; Soufi and Dalton, 2016).

Underlying these developmental decisions is the appropriate coordination of cell cycle state, as control of the timing to proliferate or arrest is pivotal to execute developmental programs (Bouldin et al., 2014; Foe, 1989; Grosshans and Wieschaus, 2000; Kurth, 2005; Matus et al., 2014; Matus et al., 2015; Murakami et al., 2004; Ogura et al., 2011). Conversely, cell cycle dysregulation is causally linked to pathogenesis, most notably the development of cancer (Hanahan and Weinberg, 2011; Kohrman and Matus, 2017; Yano et al., 2014a). Our understanding of the cell cycle dynamics underlying these decisions or how the decision to proliferate or differentiate impacts cell behavior has been limited by our ability to visualize cell behaviors and cell cycle state at high resolution *in vivo*. Fortunately, recent advances in both live cell imaging (Chen et al., 2014; Gao et al., 2014; Heppert et al., 2016; Liu et al., 2018) and the ability to rapidly tag proteins of interest in a variety of organisms (Bosch et al., 2019; Dickinson et al., 2015; Dickinson et al., 2013; Paix et al., 2015; Paix et al., 2014; Perry and

Henry, 2015) has allowed us to tackle these long-standing issues, moving beyond *in vitro* systems to the complex three-dimensional environments where cells interact with each other and the surrounding microenvironment to execute developmental programs.

The transition from mitosis to the first portion of interphase (G_1) can be easily visualized with standard light microscopy-based techniques (Bao et al., 2008; Inoue, 1953). Traditionally, distinguishing cycling cells from non-cycling cells involves the incorporation of uracil (i.e., Edu, BrdU, or other analogues) followed by fixation and visualization using secondary antibodies (Fox et al., 2011; Kocsisova et al., 2018) or click chemistry (Kuriya et al., 2016; Salic and Mitchison, 2008). In their 2008 landmark paper, Sakaue-Sawano and colleagues described a fluorescent, ubiquitination-based cell cycle indicator (FUCCI), relying on the degradation of two factors associated with DNA licensing, CDT1 and GMNN (Geminin), that have inverse expression patterns over the course of the cell cycle (Sakaue-Sawano et al., 2008). Originally employed in mammalian cell culture models, FUCCI-based systems were then developed for a variety of metazoan model systems, including fly (Zielke et al., 2014), ascidian (Ogura et al., 2011), zebrafish (Bouldin and Kimelman, 2014b; Fukuhara et al., 2014; Sugiyama et al., 2009), chicken (Esteves de Lima et al., 2014), frog (Pai et al., 2015), mouse (Abe et al., 2013; Mort et al., 2014) and most recently, *Platynereis dumerilii*, a marine polychaete (Ozpolat et al., 2017). Simultaneously, researchers have utilized FUCCI transgenic labelling to tackle a variety of cell biological questions, involving visualization of cell cycle state live during embryonic development (Abe et al., 2013; Sugiyama et al., 2009), morphogenesis (Bouldin and Kimelman, 2014b; Bouldin et al., 2014; Ogura et al., 2011; Ridenour et al., 2012) and tumor progression (Kagawa et al., 2013; Miwa et al., 2015; Yano et al., 2015; Yano et al., 2014a; Yano et al., 2014b), providing important insights into these processes.

All FUCCI-based sensors are colorimetric and generally rely on the protein degradation and activation of two transgenes, one delineating G_1 (CDT1), and the other expressed from S through mitosis (GMNN) (Sakaue-Sawano et al., 2008). The cyclic expression and rate of degradation of these transgenic products can lead to difficulties in the precise identification of cell cycle state boundaries (Koh et al., 2017; Sakaue-Sawano et al., 2017). Moreover, these limitations can prove challenging to image in cells with fast cell cycles or low transcriptional and/or translational activity. An additional limitation of the original FUCCI-based sensors is an inability to precisely distinguish between S and G_2. This has been addressed with newer FUCCI variants, which utilize additional fluorescently labeled cell cycle genes that are able to

distinguish extra cell cycle states (Bajar et al., 2016; Ford et al., 2018; Grant et al., 2018; Sakaue-Sawano et al., 2017); however, these variants require spectrally separable fluorophores for each discrete cell cycle state to be measured (Zielke and Edgar, 2015). As few labs have the equipment necessary to separate more than three or four fluorophores simultaneously, the requirement of several fluorophores to visualize cell cycle state can impede the researcher's ability to study additional cell biological behaviors by fluorescence microscopy, limiting the scope and complexity of cell cycle studies. Another limitation of existing colorimetric / degradation-based cell cycle sensors is the inability to visualize the difference between a cell that will cycle again upon completing mitosis, residing in G_1, and a cell that is quiescent or terminally differentiated, both of which are usually referred to as the G_0 phase (Buttitta and Edgar, 2007; Buttitta et al., 2010; Ma et al., 2019; Moser et al., 2018; Spencer et al., 2013). However, differentiating between these states - proliferation and quiescence - is criticall to gaining a mechanistic understanding of cell behavior during normal embryonic development, homeostasis and disease states such as cancer (Hanahan and Weinberg, 2011; Kohrman and Matus, 2017; Matus et al., 2014; Matus et al., 2015).

A ratiometric biosensor that can read out cell cycle state can overcome the limitations imposed by FUCCI-based biosensors. Rather than relying on the degradation of multiple transgenes, ratiometric biosensors (Hahn et al., 2009; Kudo et al., 2018; Regot et al., 2014; Ross et al., 2018; Spencer et al., 2013) generally utilize a phosphorylation-based system where kinase activity is measured through its ability to phosphorylate serine residues that flank a strong nuclear localization signal (**NLS**), such that, as these sites are phosphorylated the activity of a weaker Nuclear Export Sequence (**NES**) predominates, shuttling the target substrate from the nucleus to the cytoplasm. To measure cell cycle state in a quantitative fashion, a CDK2 biosensor was developed (Hahn et al., 2009; Spencer et al., 2013) that encompasses a fragment of human DNA helicase B (**DHB**) fused to a fluorescent protein, Venus, providing insight into the proliferation-quiescence decision in asynchronous mammalian cell culture (Spencer et al., 2013).

Here, taking advantage of the *C. elegans* invariant cell lineage, we present a tool to visualize the proliferation-differentiation decision in a developmental context. Through optimization of biosensor construction, we find that selection of promoter and fluorescent protein change the dynamic range of the cytoplasmic-to-nuclear ratio. We use quantitative confocal fluorescence microscopy to correlate ratiometric quantification of DHB to cell cycle state across several post-

embryonic lineages. Strikingly, visualization of CDK activity using DHB at mitotic exit allows for prediction of future cell behavior with a high degree of confidence and reproducibility, distinguishing between cycling cells in G_1 that exit with increasing CDK (**CDK^{inc}**) activity and terminally differentiated cells in G_0 that exit into a CDK low (**CDK^{low}**) state. Accurate *in vivo* identification of cell cycle state will be useful for a broad range of applications for studying differentiation and morphogenesis as well as modeling disease.

RESULTS

Generation of a live CDK biosensor in *C. elegans*

To visualize cell cycle state dynamically throughout *C. elegans* development, we first synthesized a codon-optimized fragment of human DNA Helicase B (DHB), comprised of amino acids 994-1087, fused to GFP (Hahn et al., 2009; Spencer et al., 2013). This region of DHB contains four serine phosphorylation sites flanking a strong nuclear localization signal (NLS) and is situated next to a weaker nuclear export signal (NES (Spencer et al., 2013) (Figure 1A). To simultaneously visualize the nucleus throughout the cell cycle, we generated our DHB constructs co-expressing a histone (*his-58*/H2B) fused to a second, spectrally separable fluorescent protein, which is separated from DHB using a P2A self-cleaving viral peptide. At G_0/G_1 onset, when CDK activity is low, the sensor is localized to the nucleus; however, as the cell cycle progresses and CDK activity increases, the sensor is phosphorylated, and the fraction of the sensor localized to the cytoplasm increases (Figure 1B). With both DHB and H2B co-expressed, we can utilize a nuclear mask stemming from nuclear H2B localization, which more accurately delineates the area of the nucleus compared to differential interference contrast (DIC) microscopy, alone. We then perform ratiometric quantification of the sensor by comparing the mean fluorescence intensity in the cytosol to that of the nucleus (Figure 1C).

To optimize the CDK biosensor to visualize the dynamics between proliferation and differentiation in somatic lineages, we first synthesized a codon-optimized (Redemann et al., 2011) DHB fragment with a synthetic intron fused to GFP, upstream of P2A::H2B::2x-mKate2. Next, we selected the promoter from the 40S ribosomal subunit protein S27 (*rps-27*), which is ubiquitously expressed in all cycling and terminally differentiated somatic cells during *C. elegans* development (Ruijtenberg and van den Heuvel, 2015). Using CRISPR/Cas9-genome engineering, we inserted the optimized CDK biosensor into a neutral site on chromosome I (de la Cova et al., 2017; Medwig-Kinney et al., 2019). Examination of single copy insertion lines in a

wild-type background showed consistent strong DHB::GFP and H2B::2x-mKate2 localization in all cells from mid-embryogenesis through adulthood (Figure 1D), with weaker germline expression (Figure 1D).

For quantification of the biosensor during development, we examined somatic lineages that proliferate and then undergo terminal differentiation primarily in the third and fourth larval stages post-embryonically (L3 and L4) (Kimble and Hirsh, 1979; Sulston and Horvitz, 1977). For this study, we chose three tissues of interest that proliferate during larval stages, the sex myoblasts (**SM**), the somatic gonad including the spermatheca/sheath precursors (**SS**), and ventral uterine (**VU**) cells, and the vulval precursor cells (**VPCs**) (Figure 1E). However, we were also interested in whether the biosensor could be used to distinguish cycling cells during embryogenesis. To examine this, we imaged cell divisions during embryonic gut formation, approximately 6 hours after first cleavage, in the four E16 intestinal cells (E16* cells) that divide again after the twelve neighboring E16 cells have finished their embryonic divisions (Rasmussen et al., 2013; Yang and Feldman, 2015), thereby generating the 20-celled “E20” intestine. We tracked E16* cell division from the E16 to the E20 stage and we observed that DHB::GFP localizes in a cell cycle-dependent fashion during these divisions, transitioning from nuclear to cytoplasmic localization and then re-localizing to the nucleus at the completion of cell division (Figure S1, Movie S1). Thus, DHB::GFP can be utilized during embryonic development to track cell cycle progression.

Characterizing the dynamic range of the *C. elegans* CDK biosensor

Next, we sought to examine the dynamics of the biosensor during post-embryonic development when many lineages undergo terminal differentiation after several rounds of cell division. To visualize cell cycle dynamics, we began by collecting spinning disk confocal time-lapse data, tracking the second division of the vulval precursor cells during the L3 stage over a complete cell cycle (Figure 2). For our initial characterization of the *C. elegans* version of the DHB biosensor, we fused DHB to a copy of codon-optimized GFP and used a 2x-mKate2 fusion to H2B as a nuclear mask (Figure 2A). Our observation of DHB::GFP during somatic cell divisions driven by the *rps-27* promoter revealed localization kinetics as expected, with decreasing nuclear localization as the cell cycle progressed (Figure 2A-D, Movie S2). In mammalian cell culture, using MCF10A cells, DHB::Venus is strongly nuclear excluded during G_2, with mean peak ratios of approximately 1.5 (Spencer et al., 2013). However, in our imaging of the *rps-27*>DHB::GFP transgenic line, we failed to see strong nuclear exclusion in cells prior to mitosis

in G_2, with peak values of the cytoplasmic:nuclear ratio near 1.0 (*n* = 90, 1.084 ± 0.36; Figure 2C, D).

Two main variables in the design of our version of the CDK biosensor that could contribute to a lack of strong nuclear exclusion during G_2 were the selection of promoter and/or the selection of fluorescent protein fused to DHB. To test these variables, we generated a new transgenic line expressing DHB under a different ribosomal promoter, *rps-0*, which, like *rps-27* is ubiquitously expressed, though based on quantification of publicly available RNA-seq data, at approximately 25% (3722-4078 FPKM) that of *rps-27* during the L3 and L4 stages (9019-13227 FPKM) (Celniker et al., 2009; Harris et al., 2019). Quantification of VPC division time-lapse data collected using *rps-0*>DHB::GFP revealed a higher peak value during G_2: 1.37 ± 0.45 (*n* = 33; Figure 2B-D). In support of the hypothesis that absolute levels of DHB::GFP might change the dynamic range of the biosensor, we detected a >2-fold difference in mean fluorescence intensity in the VPCs between *rps-27*>DHB::GFP and *rps-0*>DHB::GFP (543.3 ± 273.8 and 231.2 ± 83.22; Figure 2E).

The other variable that could influence the dynamic range of a ratiometric biosensor is the selection of fluorescent protein. While fluorescent protein brightness as compared to background will have a major impact on the effective dynamic range of any ratiometric sensor, in localization-based sensors, the mass of the sensor protein should also impact its dynamic range. The codon-optimized GFP we used in the generation of DHB::GFP is based on the monomeric sequence of a 26.9 kD eGFP. The synthesized codon-optimized DHB, including a nine amino acid (3xGAS) flexible linker, is predicted to be 11.2 kD (predicted by ExPASy Compute pI/MW (https://web.expasy.org/compute_pi/)) (Artimo et al., 2012), such that the DHB::GFP fusion protein is predicted to be 38.2 kD, which is below the threshold that requires active nuclear import/export machinery (Cohen-Fix and Askjaer, 2017; Timney et al., 2016). This raises the possibility that passive diffusion through nuclear pores could account for the lower dynamic range of the highly expressed *rps-27*>DHB::GFP construct.

To test this, we established a transgenic line under the control of the same ubiquitous promoter, *rps-27*, but fused to two copies of mKate2 including a 10 amino acid (2xGGGGS) flexible linker (52.8 kD). Although initially described as a monomer, reports have suggested that mKate2 behaves more like a weak dimer (Cranfill et al., 2016; Shemiakina et al., 2012). The 2x-mKate2 version of the biosensor showed strong nuclear exclusion prior to mitosis (Figure 2B).

Quantification of VPC divisions expressing DHB::2x-mKate2 showed a peak G_2 value of approximately 3.4 (n = 16, 3.445 ± 0.721; Figure 2C,D). To determine if differences between transgenes were specific to the vulval lineage, we also examined the dynamic range of the three transgenic strains during division of the SM and uterine cells (Figure S2). Similar to the VPCs, promoter strength had little effect in the SM cells (Figure S2A-C) and only slightly increased the dynamic range of the biosensor in the uterine cells (Figure S2D-F). However, the 2x-mKate2 version of the biosensor substantially increased the dynamic range in both the SM and uterine lineages, with peak values of 2.5 and 3.4, respectively (Figure S2A-F). Notably, upon inhibiting the nuclear export of DHB::2x-mKate2 through RNAi-induced depletion of *xpo-1/Exportin 1* in the uterine lineage, there was a statistically significant retention of DHB::2x-mKate2 in the nucleus relative to control (n = 45, $P \leq 1x10^{-7}$; Figure 2F, G), supporting the notion that this version of the biosensor is predominantly exported from the nucleus via active transport (Cohen-Fix and Askjaer, 2017; Timney et al., 2016). Together, these data provide strong evidence that the mass of the DHB::2x-mKate2 fusion protein decreases or limits the rate of diffusion back into the nucleus during the cell cycle, increasing the dynamic range of the biosensor.

We next quantified the DHB ratio at mitotic exit. Here, promoter strength had negligible effect in the VPCs and the choice of fluorescent protein (GFP vs. mKate2) only had a slight but significant effect on cytoplasmic:nuclear ratio following cell division in the VPCs, SM and uterine cells (VPCs: $P \leq 1x10^{-7}$, SM: $P = 3x10^{-6}$; SS/VU: $P \leq 1x10^{-7}$; Figure 2C, D and S2). In the uterine tissue, we observed a more significant effect based on fluorescent protein choice, with the 2x-mKate2 version of the biosensor having a greater mean DHB ratio following cell division of roughly 1.2 as compared to the GFP versions of the biosensor (0.51 and 0.78; Figure 2 and S2). Finally, we examined the 2x-mKate2 version of the biosensor in the germline (Figure S3A-C and Movie S3) and embryo (Figure S3E and Movie S4). Similar to the somatic tissues, we were able to easily distinguish cells in G_2 before mitosis in the germline (Figure S2A-D) and embryo (Figure S2E) as well as visualize a gradient of CDK activity across the germline from the distal mitotic region to the proximal meiotic regions (Albert Hubbard and Schedl, 2019) (Figure S2D). Thus, for ease of visualizing G_2, we recommend using the 2x-mKate2 version of the biosensor, but for visualization of CDK activity at mitotic exit during time-lapse acquisition, we advise using the transgene with the strongest signal and highest photostability, the *rps-27*>DHB::GFP strain, to balance fluorescence intensity and photobleaching. For these reasons,

we conducted the remaining experiments examining the proliferation-differentiation decision using this version of the CDK biosensor.

CDK levels after mitotic exit are predictive of terminal differentiation

In mammalian cell culture, the cytoplasmic:nuclear ratio of DHB::Venus following cell division can be used to predict whether or not a cell will remain quiescent or proliferate (Spencer et al., 2013). Cells that exit mitosis at a $CDK2^{low}$ state thus have a higher probability of staying in a G_0/quiescent cellular state than cells that exit cell division at a $CDK2^{inc}$ state (Spencer et al., 2013). As the DHB sensor in *C. elegans* appears to function in a cell cycle-dependent manner, we next wished to determine whether or not the cytoplasmic:nuclear ratio of the sensor following a cell division can be used *in vivo* to predict if a cell will divide again or terminally differentiate. Here, we can take advantage of the invariant lineage of *C. elegans* to correlate DHB ratios and CDK activity following cell divisions.

First, we quantified DHB ratios from time-lapse acquisitions of SM cell divisions. The SM cells undergo three rounds of cell division before terminally differentiating into uterine and vulval muscle (Sulston and Horvitz, 1977) (Figure 3A, B). Quantification of the first and second division of the SM cells (Figure 3C, D) revealed that these cells exit at a CDK increasing (CDK^{inc}) state ($n \geq 10$ per time point; Figure 3F). These ratios were significantly different than the DHB ratio following the third and terminal division of the SM cells (Figure 3E), where they exit at a CDK^{low} state ($n \geq 10$ per time point, $P = 4.30 \times 10^{-6}$; Figure 3F and S4). In support of these results, statistical simulations (see Methods) showed significant differences in DHB ratios between pre-terminal and terminal divisions ($P \leq 1 \times 10^{-7}$) , but no significant differences in DHB ratios in pre-terminal divisions ($n \geq 10$ per time point, P = 0.0591; Figure S4A-C).

Next, we quantified DHB ratios during the division of two somatic gonad lineages, the VU and SS cells, as they both undergo several rounds of division during the third larval stage and terminally differentiate in the early L4 stage (Sulston and Horvitz, 1977) (Figure 4A). Here, we quantified two rounds of cell divisions, including the division that leads to terminal differentiation (Figure 4C and S5A, B). Similar to the SM lineage, both somatic gonad lineages exit the round of cell division prior to their final division at a CDK^{inc} state (n = 35) and then exit CDK^{low} following their terminal differentiation (n = 13; Figure 4B, C). Similar to the SM cells, we detected a significant difference between the DHB ratios in pre- versus post-terminal divisions in the developing uterus (P = 0.00006; Figure S5C).

We next examined the divisions of the VPC lineage. The *C. elegans* vulva is derived from three cells (P5.p-P7.p), which, like the SM cells, undergo three rounds of cell division during the L3 and early L4 stages (Katz et al., 1995; Sternberg and Horvitz, 1986; Sulston and Horvitz, 1977) (Figure 5A-B, Figure S6). Rather than giving rise to 24 cells, the two D cells, the innermost granddaughters of P5.p and P7.p, terminally differentiate one round of cell division early, resulting in a total of 22 cells which compose the adult vulva (Katz et al., 1995; Matus et al., 2014; Sulston and Horvitz, 1977). Quantification of DHB ratios during VPC divisions yielded the expected pattern. The daughters of P5.p-P7.p all exited their first division at a CDK^{inc} state ($n \geq 9$ per cell type; Figure 5C, D and S6A, B). At the next division, the 12 granddaughters of P5.p-P7.p (named A-F symmetrically) are born, including the terminally differentiated D cell (Katz et al., 1995; Sulston and Horvitz, 1977) (Figure 5D). Strikingly, at this division, both by visualization from imaging and quantification of the DHB ratio, it was easy to distinguish the D cell from the remaining VPCs (Figure 5D and S6C), as the D cell exited and remained in a CDK^{low} state ($n = 10$), while the remaining VPCs exited at a CDK^{inc} state ($n \geq 9$ per cell type) and continued to cycle (Figure 5C and S6C). All remaining VPCs exited into a CDK^{low} state ($n \geq 9$ per cell type; Figure 5C, D and S6D) at their final terminal division.

Again, results from statistical simulations (See methods, Figure S7) failed to detect significant differences between DHB ratios of pre-differentiated VPCs (For all comparisons, $P > 0.05$, Figure S7D-G), with the exception of the birth of the C and D cells from the CD mother cell ($P = 0.002208$, Figure S7E). Here, the D cell exited CDK^{low}, while the C cell exited at a CDK state that lies between the other VPCs (A/B/E/F) and the terminally differentiated D cell ($n \geq 9$ per cell type; Figure S7), statistically distinct from both its sister D Cell's CDK^{low} state ($P = 0.002208$) and from its cousin A, B E and F cells ($P = 0.008287$). However, within 30 minutes following the birth of the C cell, we could detect a significant difference between the C and D cells ($P = 0.020$), and by 90 minutes there was no significant difference between the C cell and cousin A/B/E/F cells ($P > 0.05$; Figure S7G). Despite this subtle difference between the C cell and its cousins, the DHB biosensor can accurately predict future cell behavior. Thus, for all three somatic lineages, we can visually and statistically distinguish the difference between a cell that completes mitosis and exits a cell division in G_1 and will continue to cycle versus a cell that exits mitosis into a terminally differentiated G_0 state.

As our data from the DHB biosensor correlated precisely with the invariant lineages we examined during *C. elegans* post-embryonic development, we next sought to test whether the biosensor could be used to quantitatively readout cell cycle perturbation. To accomplish this, we generated a transgenic line with BFP-tagged CKI-1 (p21/p27 homolog) under an inducible heat shock promoter (*hsp*>CKI-1::2xTagBFP2) paired with an mKate2 version of the DHB biosensor (*rps-0*>DHB::mKate2). Induced expression of a cyclin-dependent kinase inhibitor (CKI) in any lineage should result in a temporary G_0 arrest (Hong et al., 1998; Matus et al., 2014; van der Horst et al., 2019). Indeed, in both the SM and VPC lineages, induced expression of CKI-1 resulted in cells entering a CDK^{low}/G_0 state, with mean DHB ratios of 0.1 ± 0.05 and 0.11 ± 0.05, respectively, ($n \geq 36$ cells per treatment; Figure 6A, B and S8) as compared to control animals that lacked heat shock-induced expression (VPC ratio = 0.46 ± 0.87; SM ratio = 0.99 ± 0.82) or lacked the inducible transgene (VPC ratio = 0.47 ± 0.42; SM ratio = 0.96 ± 0.77; Figure 6A, B). Thus, induced G_0 arrest by overexpression of CKI-1 is functionally equivalent, by CDK activity state, to G_0 arrest that occurs following mitotic exit in a terminally differentiated cell.

In mammalian cell culture, CDK2 activity is predictive of future cell behavior (Moser et al., 2018; Overton et al., 2014; Spencer et al., 2013), suggesting a bifurcation at mitotic exit based on DHB ratiometric quantification. To test if this is also the case *in vivo* during *C. elegans* development, we plotted all DHB trace data quantified from time-lapse data, irrespective of lineage, aligned to anaphase (Figure 6C). We found that cells that exited cell division at a CDK^{low} state were primarily from traces of terminally differentiated cells ($n = 154$), while cells that exited mitosis at a CDK^{inc} state represented trace data from pre-terminal divisions ($n = 127$, $P \leq 1x10^{-7}$). Thus, these results are consistent with mammalian cell culture, supporting a model that during *C. elegans* development, cycling cells must cross a bifurcation point following mitosis based on CDK activity, where they either immediately increase CDK activity and are poised to cycle or exit into a CDK^{low} state and undergo terminal differentiation.

DISCUSSION

In this report we present the generation and characterization of a CDK ratiometric biosensor based on the CDK2 phosphorylation domain of human DNA Helicase B (DHB) (Hahn et al., 2009; Spencer et al., 2013) capable of distinguishing all interphase cell cycle states throughout the life cycle of *C. elegans*, including the G_0 phase of the cell cycle. In mammalian cell culture, DHB as a CDK2 biosensor has been a useful tool to visualize the difference between

proliferative and quiescent cells in asynchronous cell populations (Arora et al., 2017; Cappell et al., 2016; Gast et al., 2018; Gookin et al., 2017; Miller et al., 2018; Moser et al., 2018; Overton et al., 2014; Spencer et al., 2013; Yang et al., 2015). This has prompted researchers to define a new cell cycle restriction point as a bifurcation point immediately following mitotic exit based on CDK2 activity, with proliferative cells exiting at a CDK2 increasing ($CDK2^{inc}$) state and quiescent cells exiting at a CDK2 low ($CDK2^{low}$) state (Spencer et al., 2013). Recent studies using primary fibroblasts and serum removal argues for a more traditional threshold-based model and raises the possibility that DHB reads out both CDK1 and CDK2 activity (Schwarz et al., 2018). Regardless, both models posit that single CDK biosensor-based measurements can be used to accurately predict cell behavior and the proliferation-quiescence decision *in vitro*. While these conflicting models have been developed in similar tissue culture paradigms, whether cells *in vivo* respond to CDK activity in a threshold-dependent manner or not is poorly understood. Here, by quantifying the cytoplasmic-to-nuclear ratio of the DHB biosensor in time-lapse recordings of cell divisions in *C. elegans* somatic lineages we can distinguish two populations of cells in G_0/G_1; the first being terminally differentiated cells in a CDK^{low} state (G_0), and the second being actively cycling cells in a CDK^{inc} state (G_1). Combined with the invariant lineage of *C. elegans*, this will be a powerful tool for dissecting cell cycle regulation of cell behaviors during development and homeostasis.

In the generation of a ratiometric biosensor that can be used to quantify cell cycle state dynamically throughout *C. elegans* development, we have carefully explored the interplay between promoter strength and choice of fluorescent protein. Our work extends previous studies using DHB in tissue culture (Spencer et al., 2013) and *C. elegans* (van Rijnberk et al., 2017). A previous transgenic strain of DHB::GFP generated in *C. elegans* using the *mcm-4* promoter (van Rijnberk et al., 2017) was also shown to localize in a cell cycle-dependent fashion, reading out CDK activity and was recently used to examine an S-phase dependent cell extrusion event during embryogenesis (Dwivedi et al., 2019). As the *mcm-4* promoter does not maintain expression in differentiated cells we selected ribosomal subunit promoters (*rps-27* and *rps-0*) to drive the ubiquitous expression of DHB at all life history stages, in order to examine the proliferation-differentiation decision. We show here that specific molecular features of our biosensor, such as overall sensor mass and choice of fluorophore, are important in terms of tuning the expression levels and dynamic range of the sensor. When generating cytoplasmic-to-nuclear localization-based sensors, the diffusion kinetics and mechanics of nuclear transportation of the probe should be considered to optimize the dynamic range of the sensor.

Additionally, levels of expression should be tuned by both adjusting promoter strength and the stability of RNAs to drive optimal expression in *C. elegans* (Redemann et al., 2011). Together, our data show that rational design of ratiometric biosensors can optimize utility for live cell imaging.

Cell cycle state sensors have been used for the last decade in tissue culture and *in vivo* to provide new insights into underlying cell biology. Various cell cycle sensors have been developed, starting with FUCCI in 2008 (Sakaue-Sawano et al., 2008), each optimized for different research paradigms (Abe et al., 2013; Bouldin and Kimelman, 2014b; Fukuhara et al., 2014; Ogura et al., 2011; Pineda et al., 2016; Ridenour et al., 2012; Sakaue-Sawano et al., 2017; Sugiyama et al., 2009; Zielke et al., 2016). While FUCCI-style biosensors have been developed to better assess G_0/G_1 in zebrafish using inactivated p27 (Oki et al., 2014), and in tissue culture by assessing the primary cilium cycle (Ford et al., 2018), they require multiple transgenes to readout cell cycle states accurately. As DHB responds to CDK levels, it is likely to function broadly across a wide range of organisms. This broad functionality will allow for new discoveries that address major scientific questions, such as the interplay between cell cycle state and tissue regeneration and reprogramming, the cell cycle regulation of morphogenetic behaviors, and new insights into the mechanisms of diseases arising from cell cycle defects.

COMPETING INTERESTS

The authors declare no competing interests.

FUNDING

This work was funded by the National Institute of Health (NIH) National Institute of General Medical Sciences (NIGMS) [1R01GM121597-01 to D.Q.M.]. D.Q.M. is also a Damon Runyon-Rachleff Innovator supported (in part) by the Damon Runyon Cancer Research Foundation [DRR-47-17]. R.C.A. and A.Q.K. are both supported by the NIGMS [1F32133131-01 and F31GM128319-01 respectively]. J.J.S. and M.A.Q.M. are also both supported by the NIGMS [3R01GM121597-02S1 and 3R01GM121597-02S2, respectively]. T.N.M. is supported by the National Institute of Child Health and Human Development (NICHD) [F31HD100091-01]. N.J.P. is supported by the American Cancer Society [132969-PF-18-226-01-CSM]. Some strains were provided by the Caenorhabditis Genetics Center, which is funded by the NIH Office of Research Infrastructure Programs (ORIP) [P40 OD010440].

ACKNOWLEDGEMENTS

We thank L. Lapierre for the *xpo-1* RNAi clone. We thank B. Martin and D. Pisconti (Stony Brook University) for helpful comments on the manuscript. We thank S. Spencer (University of Colorado Boulder) for thoughtful discussions on the project. We also thank J. Maghakian and L. Yang (Stony Brook University) for consultation on statistical modeling. Additional thanks to D. Dickinson (University of Texas at Austin) and B. Goldstein (University of North Carolina at Chapel Hill) for assistance with design and execution of the CRISPR single copy knock-in strategy described and used in this manuscript. We also thank T. Geer (Nobska Imaging, Inc.) for assistance in setting up and maintaining our spinning disk confocal microscopes. A. Kohrman is grateful for the computational training he received at the CIAN at the MBL, which was supported by NIGMS.

EXTENDED EXPERIMENTAL PROCEDURES

C. elegans Culture Conditions, Handling and Strains

C. elegans strains were cultured in standard conditions at 15-25°C on NGM plates with *Escherichia coli (E. coli)* strain OP50, as previously described (Brenner, 1974). Wild-type *C. elegans* animals were strain Bristol N2. In the text and figures, we designate linkage to a promoter with a greater than symbol (>) and use a double colon (::) for linkages that fuse open reading frames (Ziel et al., 2009). Animals were synchronized for experiments via hypochlorite treatment and fed on bacterial lawns of *E. coli* (strain OP50). The following alleles and transgenes were used: **LGI** *bmd86[LoxP::rps-27>DHB::GFP::P2A::H2B::mKate2]*, *bmd129[LoxP::hsp-16-41>CKI-1::2xBFP], bmd147[rps-27>DHB::2x-mKate2::P2A::H2B::GFP]*, *bmd162[rps-0>DHB::GFP::P2A::H2B::2x-mKate2]*; **LGII** *bmd118[LoxP::rps-0>DHB::mKate2]*.

C. elegans Transgenic Strain Generation

Transgene insertion was performed via CRISPR/Cas9 genome engineering to generate single copy knock-ins to a known neutral locus on either chromosome I or II using a self-excising cassette (SEC)-based method, as described previously (de la Cova et al., 2017; Dickinson et al., 2015). Homologous repair templates and guide plasmids were graciously provided by Bob Goldstein and target the mosSCI integration sites ttTi4348 and ttTTi5605 on chromosome I and II, respectively. All CRISPR microinjection products were prepared using a Purelink HQ DNA Purification Kit (Thermo-Fisher/Invitrogen #K210001) with the inclusion of an additional wash step prior to the final ethanol wash of the column, using 650 µL of 60% 4M guanidine hydrochloride (Fisher: #BP178-500) (pH 6.5 / 40% isopropanol). All purified microinjection products were stored at 4˚C. Injection mixes were made fresh before each round of injection and contain: Cas9-sgRNA plasmids (50 ng/µL), homologous repair templates (50 ng/µL), and a co-injection marker (pCFJ90, 2.5 ng/µL). Injection mixes were injected into the gonads of young adult *C. elegans* N2 animals, and successful integrants were identified in the F3 offspring of injected animals following the protocol established in (Dickinson et al., 2015). Briefly, injected young adult hermaphrodites of the relevant parent strain were each individually transferred to a fresh OP50 plate, and allowed to lay eggs for 3 days at 25˚C. On Day 3, 400 µL of hygromycin B (EMD Millipore #400052) from a 5 mg/mL stock was added to the plates to a final concentration of 0.25 mg/mL. After five days of hygromycin B exposure, surviving dominant *sqt-1* roller (Rol) worms were singled out onto fresh OP50 plates, checked for expression of the desired transgene/genomic edit and/or the presence of extrachromosomal array markers on a

fluorescence dissecting microscope (Frame and Automation: Axiozoom.V16(Zeiss), Light source: Sola Light Engine (Lumencor)). The RoI phenotype was assessed for Mendelian inheritance, and if possible, the genomic edit was homozygosed. Once homozygosed, selectable markers (hygromycin B resistance and dominant *sqt-1* RoI phenotype) were removed from the genome using heat shock inducible Cre-Lox recombination via an overnight (8 – 18 hour) heat shock of large numbers of L1 and L2 stage animals at 30˚C in an air incubator (VWR #89611-416). After two days, wildtype worms were singled out one to a plate. Additional strains were provided by the CGC. A list of all *C. elegans* strains reported, their genotypes and method of generation can be found in the Key Resource Table.

Molecular Biology

Synthetic DNAs were ordered as either gBlocks from IDT or gene fragments from Twist Bioscience (see Key Resources Table for details). The nucleotide sequence of DHB (index 1.0) was codon optimized for somatic expression and the P2A (index 0.2) sequence de-optimized to increase the efficiency of ribosome stalling in *rps-27>DHB::2x-mKate2::P2A::H2B::GFP*) using https://worm.mpi-cbg.de/codons/cgi-bin/optimize.py (Redemann et al., 2011). The *C. elegans rps-0* and *rps-27* promoters were amplified from N2 genomic DNA. Sequences of all primers and synthetic DNAs are provided in the relevant appendix. Synthetic gene fragments and amplified DNAs were cloned via Gibson Assembly (Barnes, 1994; Gibson et al., 2010; Gibson et al., 2009) or NEBuilder HiFi (NEB) into target plasmids (see Key Resources Table for details).

Microscopes

Microinjections for *C. elegans* transgenesis were performed on an injection setup combining a Zeiss Axio Observer A1 inverted compound frame, EC Plan-Neofluar 40x/0.75 NA DIC objective and floating stage, with a Narashige manual micromanipulator and a picoliter injection system from Warner for fine control of delivered volume. Microinjection needles were pulled on a Sutter P-97 reconditioned and calibrated by Sutter.

All *C. elegans* imaging, excluding the animals presented in Figures 1, S1 and S3, was performed on a custom-assembled spinning disk confocal microscope consisting of a Zeiss Imager A.2 frame, a Borealis modified Yokogawa CSU-10 spinning disc, ASI 150uM piezo stage controlled by an MS2000, and ASI filter wheel, and a Hamamatsu ImageEM x2 EMCCD camera (Hamamatsu C9100-23B). The imaging objective used for all *C. elegans* experiments was a Plan-APOCHROMAT 100x /1.4 NA DIC objective (Carl Zeiss). Laser illumination was provided

via a 405/442/488/514/561/640 nm Vortran laser merge driven by a custom Measurement Computing Microcontroller integrated by Nobska Imaging. This microscope was controlled with Metamorph microscope control software (V7.10.2.240 Molecular Devices), and laser power levels were set in Vortran's Stradus VersaLase 8 software.

The animals presented in Figure 1 were imaged on a custom assembled spinning disk confocal microscope consisting of an automated Zeiss frame, a Yokogawa CSU-10 spinning disc, a Ludl stage controlled by a Ludl MAC6000 and an ASI filter turret mated to a Photometrics Prime 95B camera. Imaging for all *C. elegans* experiments on this microscope used a Plan-APOCHROMAT 63x/ 1.4NA DIC objective (Carl Zeiss). Laser illumination was provided by a six line, 405/442/488/514/561/640 nm Vortran laser merge driven by a by a custom Measurement Computing Microcontroller integrated by Nobska Imaging. This microscope was also controlled with Metamorph microscope control software (V7.10.2.240 Molecular Devices), and laser power levels were set in Vortran's Stradus VersaLase 8 software. Custom integration and maintenance for both systems performed by Nobska Imaging. Zeiss components were installed and serviced by MicroOptics.

For the data presented in Figure S1, live *C. elegans* embryo imaging was performed on a Nikon Ti-E inverted microscope (Nikon Instruments, Melville, NY) using a 60xOil Plan Apochromat (NA = 1.4) objective and controlled by NIS Elements software (Nikon). Images were acquired with an Andor Ixon Ultra back thinned EMCCD camera using 488 nm or 561 nm imaging lasers and a Yokogawa X1 confocal spinning disk head equipped with a 1.5Å magnifying lens.

For time-lapse of the germline and embryos in Figure S3 and Movies S3, 4) images were acquired using a Yokogawa CSU-W1 SoRa spinning disk confocal in SoRa disk mode with 1.0x relay lens, a 60x/1.27 NA water immersion objective, and a Prime 95B sCMOS camera mounted on a Nikon Ti-2 stand. Nikon Elements AR software was used for image acquisition, and images were processed for figures using FIJI (version: 2.0.0-rc-69/1.52p).

C. elegans Imaging Conditions

For all experiments, static, single time point, imaging was performed on *C. elegans* anesthetized via mounting on an agar pad containing sodium azide (#S8032) (Matus et al., 2015). Time-lapse imaging of *C. elegans* was performed using a protocol modified from (Kelley et al., 2017), substituting a 22 mm square coverslip #1.5 (Fisher Scientific #12-541-B), and dividing the

imaging agar pad into two, asymmetric, smaller portions (each 2-3 mm square) and filling the void space under the coverslip with additional M9 buffer. These modifications allowed for much longer imaging durations and substantially reduced sample Z-drift over the course of the imaging session on both upright and inverted microscope systems. For some experiments a 0.1% tricaine (Sigma #E10521) / 0.01% levamisole ((−)-Tetramisole hydrochloride (Sigma #L9756) anesthetic (Kirby et al., 1990; Maddox and Maddox, 2012; Wong et al., 2011) was substituted for 5mM levamisole in M9 buffer. In order to maintain animals in an anesthetic state for long-duration time-lapse imaging, imaging chambers were flooded with 5 mM levamisole in M9 instead of M9.

Embryos for imaging (Figure S1, S3 and Movies S1, S4) were collected by dissection from gravid hermaphrodites and incubated for 4 - 4.5 hours in M9 at room temperature (Figure S1 and Movie S1) or imaged immediately (Figure S3 and Movie S4). For live imaging, images were taken at a sampling rate of 0.5 µm. For time-lapse, Z-stacks were collected every four (Figure S1 and Movie S1) or three minutes (Figure S3 and Movie S4).

For time-lapse of the germline (Figure S3 and Movie S3) young adult animals were lightly immobilized using 0.1 mM levamisole in M9 buffer and mounted on 5% agarose pads.

C. elegans RNAi Perturbations

RNAi was delivered by feeding *E. coli* feeding strain HT115(DE3) expressing double-stranded RNA (dsRNA) (Fire et al., 1998) to synchronized L1 stage strains containing the following transgenes: **LGI** *bmd162[rps-0>DHB::GFP::P2A::H2B::2x-mKate2].* Transcription of dsRNA was induced with 1mM Isopropyl b-D-1-thiogalactopyranoside (IPTG) in bacterial cultures, which were plated on NGM plates induced with 5 µl each of 30 mg/mL carbenicillin and 1M IPTG (Kelley et al. 2019). The RNAi vector targeting *xpo-1* was graciously provided for use in this study by L. Lapierre, and originally obtained from the *C. elegans* ORF-RNAi library (Source BioScience) (Rual et al., 2004). The empty vector L4440 was used as a negative control. All RNAi vectors were verified by Sanger sequencing.

Computational resources

For data analysis and statistical simulation two workstation computers were used. The first system consists of an I9-9900X processor (Intel), an Nvidia GeForce GTX1070 Ti GPU (Nvidia), 128 GB of DDR4 RAM (Corsair), and data being used for computation was stored on a 4 TB

RAID0 array consisting of two 2 TB drives (Samsung). Both systems boot into Windows 10 (Microsoft) off a 1 TB M.2 drive (Samsung 970 EVO Plus). The second system has an I9-9900K processor (Intel), EVGA GEFORCE RTX 2070 GPU (Nvidia) and 64 GB of DDR4 RAM (G.Skill Ripjaw). Data were stored on a 2 TB RAID0 array consisting of two 1 TB Drives (Samsung). System integration, support and maintenance performed by Nobska Imaging.

Image Collection Software

As described in the previous section, Metamorph (Molecular Devices) or Nikon Elements (Nikon) microscope control software was used to collect all data. Initial data review was performed in FIJI (Schindelin et al., 2012).

Image Processing and Analysis

Hand quantification of images was performed in FIJI. Due to the high level of amplifier noise in EMCCD images, and to remove any remaining out-of-focus fluorescence in these confocal micrographs, a rolling ball background subtraction was used, with a size of 50 (Sternberg and Corporation, 1983). After a recording was qualified for inclusion, ratiometric measurements were obtained.

First, the Z plane containing the center of the cell of interest was located. Using the freehand tool, a conservative toroid was drawn around the nucleus and excluding the nucleolus if present. The fluorescent histone and corresponding DIC and DHB images were used to assess the accuracy of this toroid. A measurement of mean grey value was obtained. Then, a region of perinuclear cytoplasm was chosen so as not to include pixels which might belong to the cytoplasm of neighboring cells. The mean grey value of the cytoplasmic patch was then measured. These values were recorded, and a cytoplasmic/nuclear ratio was calculated. If there were multiple cells of interest in the image, the procedure was repeated for each cell. For time-lapse recordings this procedure was then repeated at each time point.

Data Organization and Storage

Data from hand quantification were organized and stored in Excel spreadsheets (Microsoft), or, for ease of collaboration, in Google Sheets spreadsheets (Google). Time series data were organized by cell type and treatment.

Figure Generation

Data for figures were plotted in Graph Pad Prism (version: 8.1.2). Micrographs in all figures were reviewed and selected in FIJI. Figure micrographs were contrast and brightness adjusted for ease of display, in Adobe Photoshop CC (version: 20.0.6) or FIJI. Figures were assembled in Adobe Illustrator CC (version: 23.0.26).

Generation of Supplemental Movies

Supplemental movies were selected in FIJI and clipped to the desired length. The plane of interest was selected in FIJI and a time-lapse montage of channels was created. Time-lapse movies were rotated to standard orientation, cropped to the relevant region and timestamps and scale bars annotations were added in FIJI. For ease of viewing brightness and contrast were adjusted. Movies showing more than one channel were assembled using the multi-stack montage plugin

Statistical Tests

Statistical Simulations were performed in Matlab R2019A. The code used for statistical simulations is available upon request. Custom code for this manuscript may not be compatible with Matlab releases older than R2019A.

Statistical Simulations

When single timepoint samples did not exhibit normal distributions, empirical statistics were calculated. For single timepoint experiments, a bootstrapped distribution of the difference between mean groups was calculated for each comparison. 10^8 statistical simulations were performed by random sampling without replacement in Matlab. P value was calculated by determining the proportion of simulated differences with values greater than the true difference.

For comparisons of time course data, a different technique was utilized. For each comparison, traces for the cell types to be compared were collected, and a mean trend line was calculated for each. The area under each trendline was calculated, for the desired time window, and the difference calculated ($\int_{t_0}^{t_n} f(t) - \int_{t_o}^{t_n} g(t)$). Then, statistical simulations were performed by random partitioning of the data without replacement into two groups with the same sizes as the original groups. Mean trendlines were then calculated for these randomly assigned groups, and $1x10^7$ simulated replicates were performed to estimate the sampling distribution of the

difference statistic. *P* value was calculated by determining the proportion of simulations with more extreme statistical values (see Figure S9 for detailed schematic).

Reporting of Statistical Results

Exact *P* values and *n* (number of cells) are reported throughout the study unless otherwise specified. *P* values for comparisons are reported in figure legends and relevant body of the manuscript. For statistical comparisons performed using empirical distributions, plots of distribution for each comparison are available upon request.

In the course of data collection for this manuscript, many animals were recorded that were not included in this manuscript. In order to be considered for analysis recordings, they had to satisfy the following criteria: (1) A cell of interest had to have been present in the recording. (2) The cell of interest must have exhibited at least one anaphase during the recording. (3) The animal must have appeared physiologically normal at the beginning and end of the recording. Additional criteria for exclusion were the presence of a stalled metaphase plate at any point in the movie or unexpected developmental arrest.

Figure 1

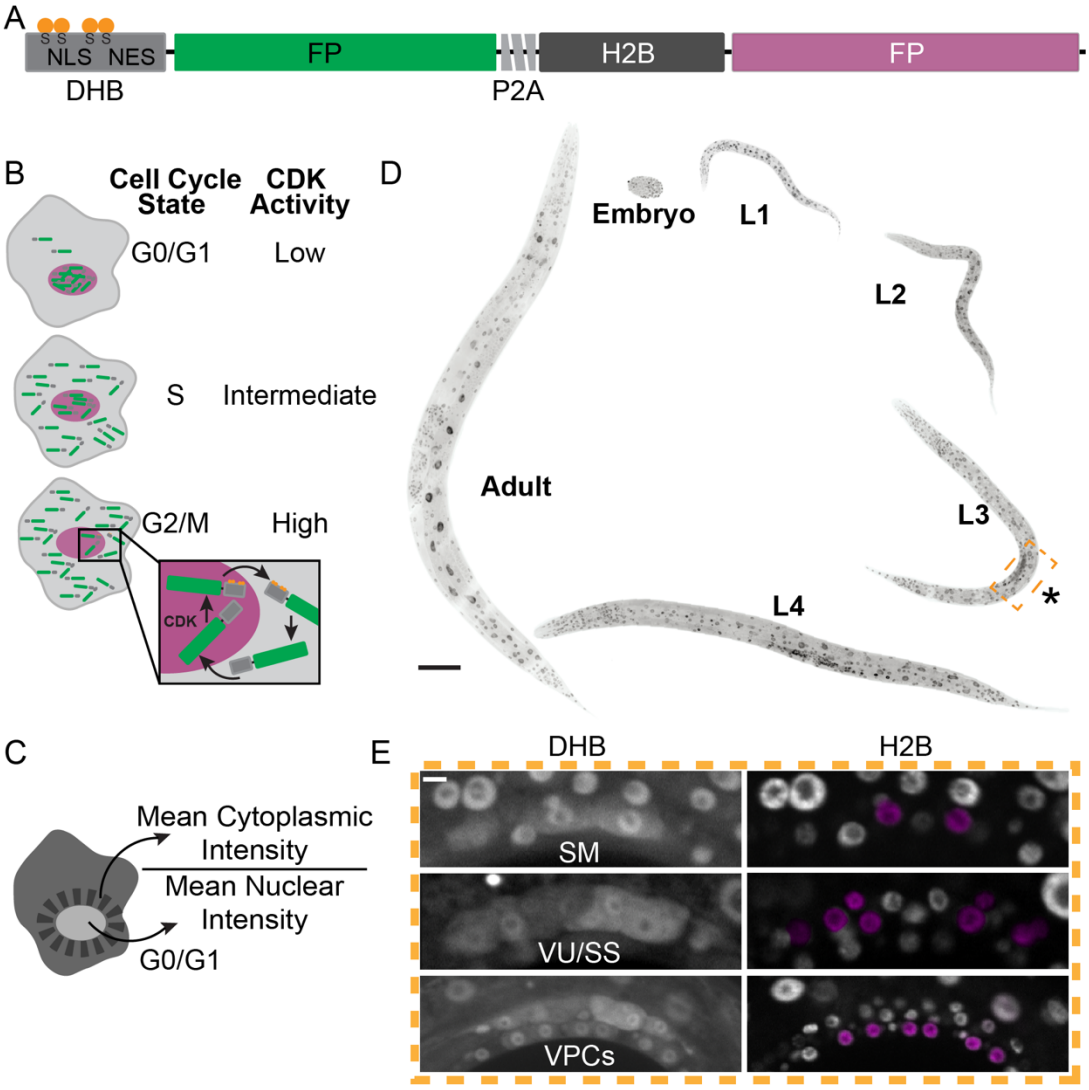

Figure 1. Generation of a CDK biosensor for live cell cycle visualization in *C. elegans*. (A) The CDK biosensor is comprised of a fragment (AA 994-1087) of human DNA Helicase B (DHB) fused to a fluorescent protein (FP) and a nuclear mask (H2B::FP) separated by a self-cleaving peptide (P2A). DHB contains a nuclear-localization signal (NLS) flanked by four serine phosphorylation sites and a nuclear export signal (NES). (B) In CDK^{low} states, the NLS predominates and the biosensor is nuclear-localized. As CDK activity increases during cell cycle progression and DHB is phosphorylated, the NLS becomes occluded and the NES prevails, displacing the biosensor to the cytoplasm. (C) Cell cycle state is quantified by measuring the ratio of mean fluorescent intensity in the cytoplasm to that in the nucleus. (D) The DHB biosensor (*rps-27*>DHB::GFP::P2A::H2B::mKate2) is expressed robustly throughout *C. elegans*

development. Images shown as inverted for display purposes. Scale bar = 100 μm. (E) Visualization of DHB expression in sex myoblasts (SM), ventral uterine and spermatheca/sheath precursor cells (VU/SS), and vulval precursor cells (VPCs). The nuclei (H2B) of each lineage are highlighted in magenta. Scale bar = 5 μm.

Figure 2

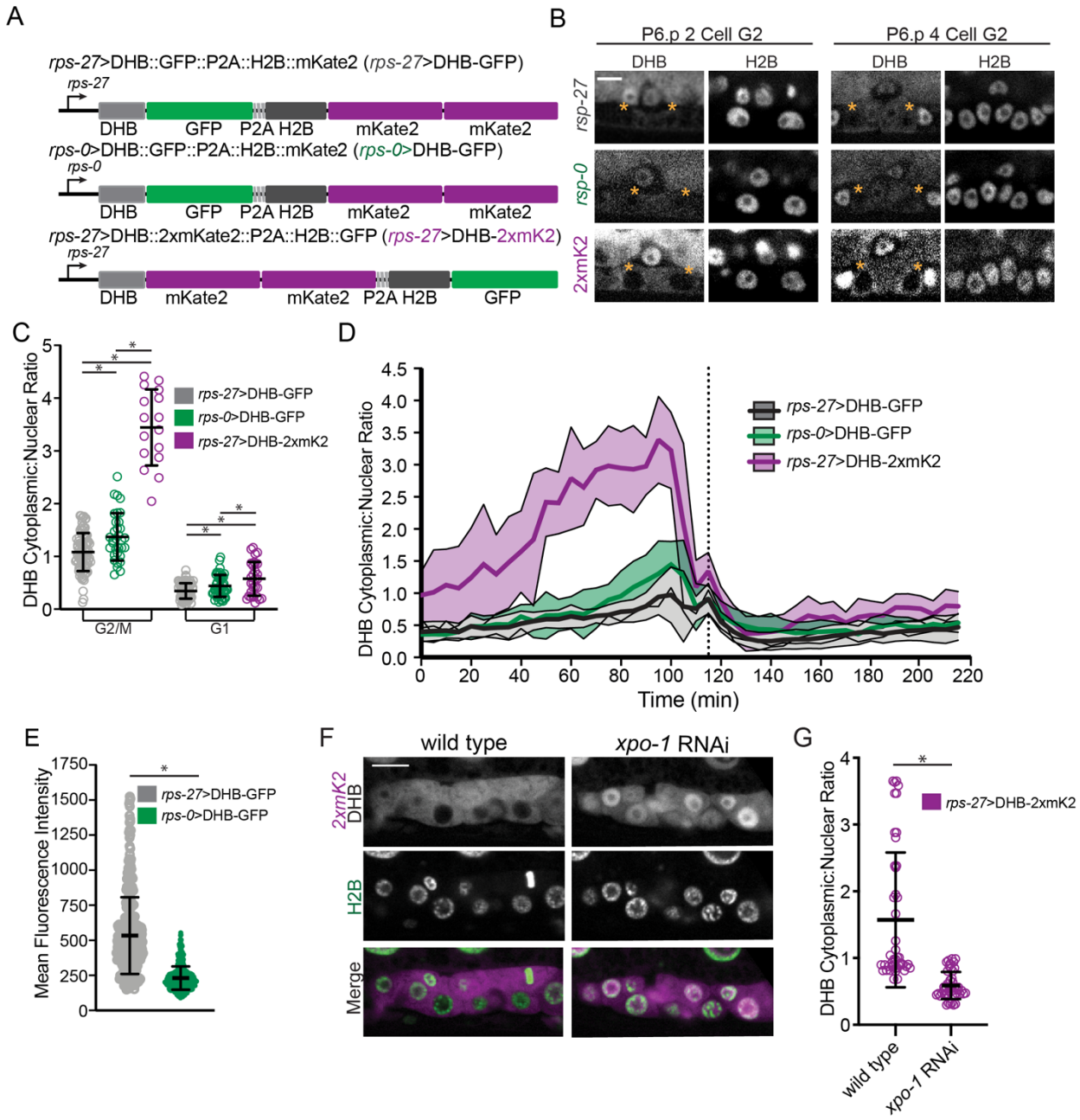

Figure 2. Ratiometric biosensor dynamic range varies with promoter and fluorescent protein. (A) Schematic of DHB biosensors engineered using different combinations of ubiquitous promoters (*rps-27* or *rps-0*) and fluorescent proteins (GFP or 2x-mKate2). (B) Representative images of biosensor expression and localization in G_2 phase within the P6.p lineage at the 2-cell and 4-cell stage. (C) Dot plot depicting dynamic ranges of the three DHB biosensor variants, measured by the cytoplasmic:nuclear ratio of DHB mean fluorescent intensity, at G_2/M and G_1 phases ($n \geq 16$, G_2 : *rps-27>DHB::GFP vs rps-0>DHB::GFP* *P =

0.0002200; *rps-27>DHB::GFP* vs *rps-27>DHB::2xmK2* $*P \leq 1x10^{-7}$; *rps-0>DHB::GFP* vs *rps-27>DHB::2xmK2* $*P \leq 1x10^{-7}$; G_1: *rps-27>DHB::GFP* vs *rps-0>DHB::GFP* $*P = 0.009664$; *rps-27>DHB::GFP* vs *rps-27>DHB::2xmK2* $*P \leq 1x10^{-7}$; *rps-0>DHB::GFP* vs *rps-27>DHB::2xmK2* $*P = 0.000331$;). (D) Time series of DHB localization in cycling cells over time, measured every 5 minutes ($n \geq 21$ per strain). (E) Dot plot comparing overall intensity and dynamic range of *rps-27* and *rps-0* driven constructs ($n \geq 388$, $*P \leq 1x10^{-7}$). (F, G) Representative images (F) and quantification (G) of DHB biosensor localization with and without perturbations to nuclear export activity via *xpo-1* RNAi treatment ($n = 45$ per treatment, $*P \leq 1x10^{-7}$). Scale bar = 5 μm. Dotted line indicates time of anaphase. Error bars and shaded error bands depict mean ± standard deviation.

Figure 3

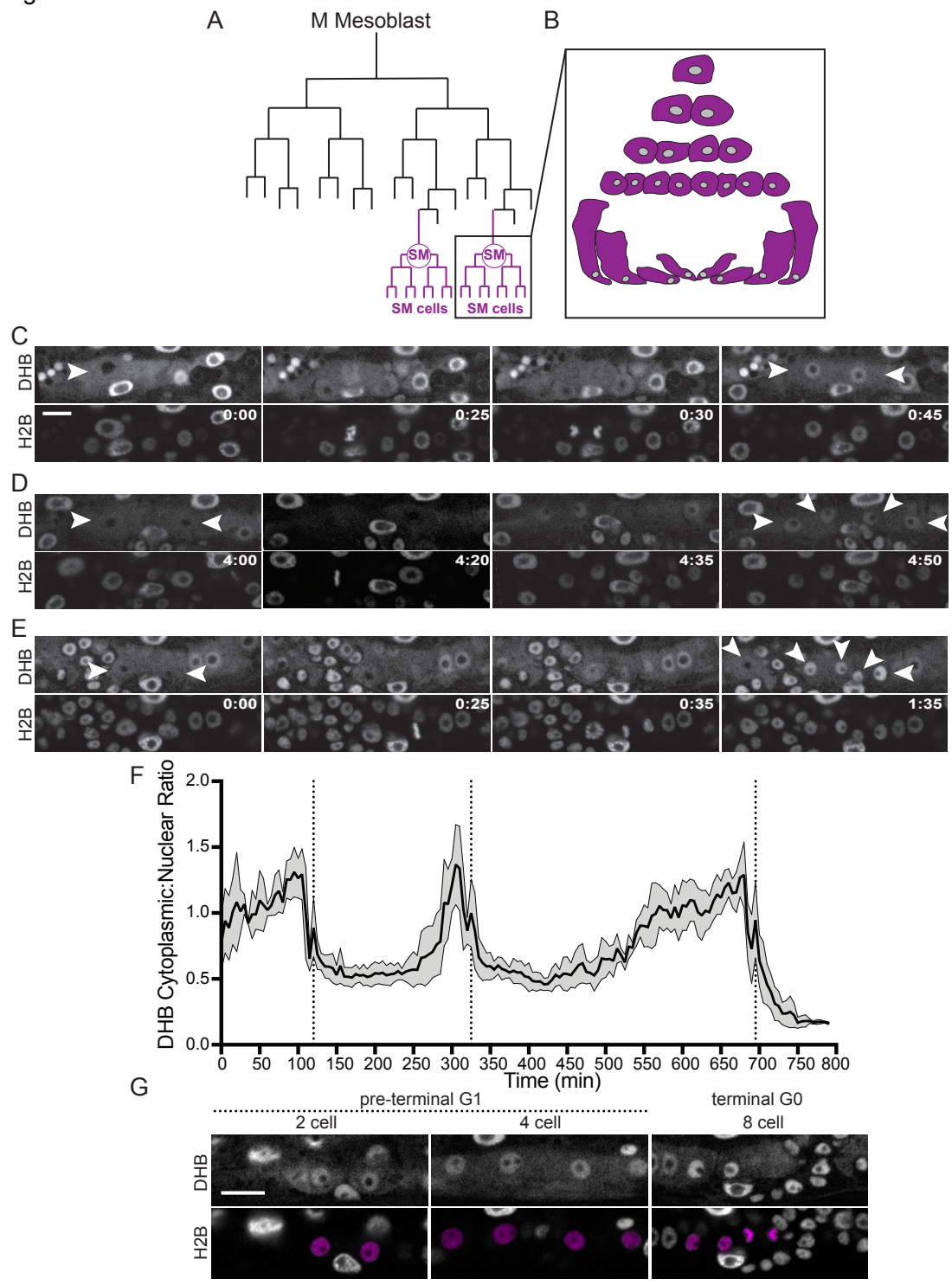

Figure 3. Sex myoblasts exit terminal divisions into a CDK^{low} state. (A) Simplified schematic of the cell lineage that gives rise to the sex myoblast (SM) cells. (B) The SM cells undergo three rounds of cell division before terminally differentiating. (C-E) Still micrographs of a time-lapse movie showing SM cells dividing from 1 cell to 2 cells (C), 2 cells to 4 cells (D), and finally 4 cells to 8 terminally differentiated cells (E). (F) Time series of DHB biosensor localization in SM cells over time, as measured every 5 minutes. Scale bar = 10 μm ($n \geq 10$). (G) Representative images of DHB biosensor localization in pre-terminal/G_1 and terminal/G_0 stage SM cells. Dotted line indicates time of anaphase. Shaded error bands depict mean ± standard deviation.

Figure 4

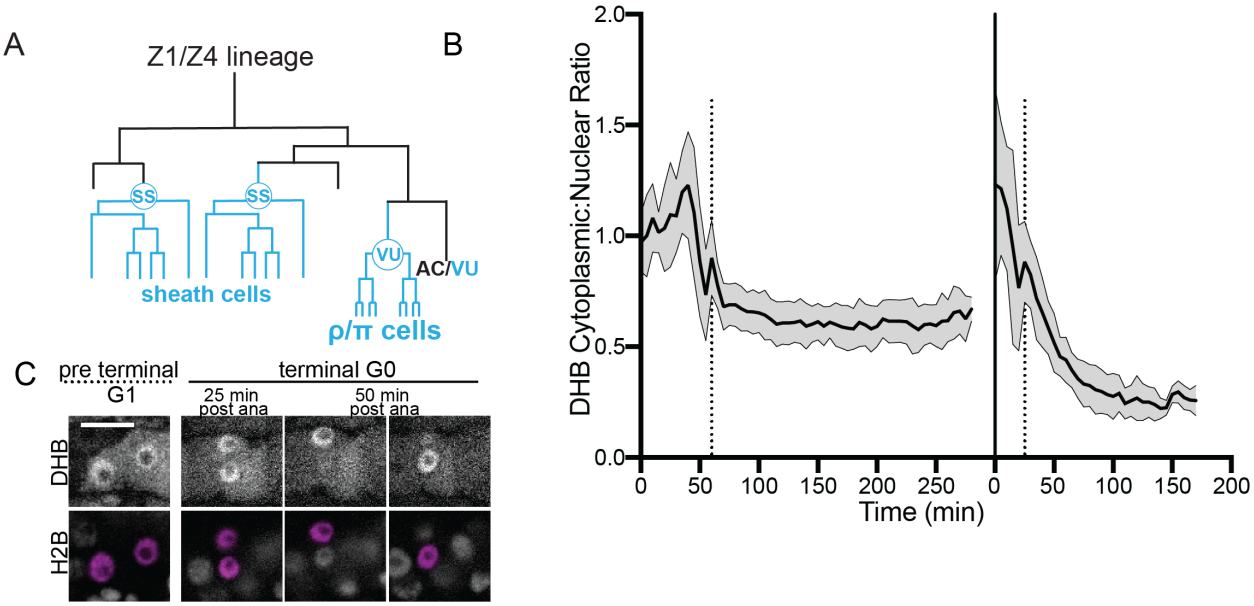

Figure 4. Uterine cells exit terminal divisions into a CDK^{low} state. (A) Simplified schematic of the cell lineage that gives rise to the spermatheca/sheath precursors (SS) and ventral uterine (VU) cells. (B) Time series of DHB biosensor localization in SS and VU cells over time, as measured every 5 minutes ($n \geq 13$). (C) Localization of the DHB biosensor in SS cells in a pre-terminal/G_1 state compared to those in a terminal/G_0 state, indicated by time post-anaphase (ana). Scale bar = 10 μm. Dotted line indicates time of anaphase. Shaded error bands depict mean ± standard deviation.

Figure 5

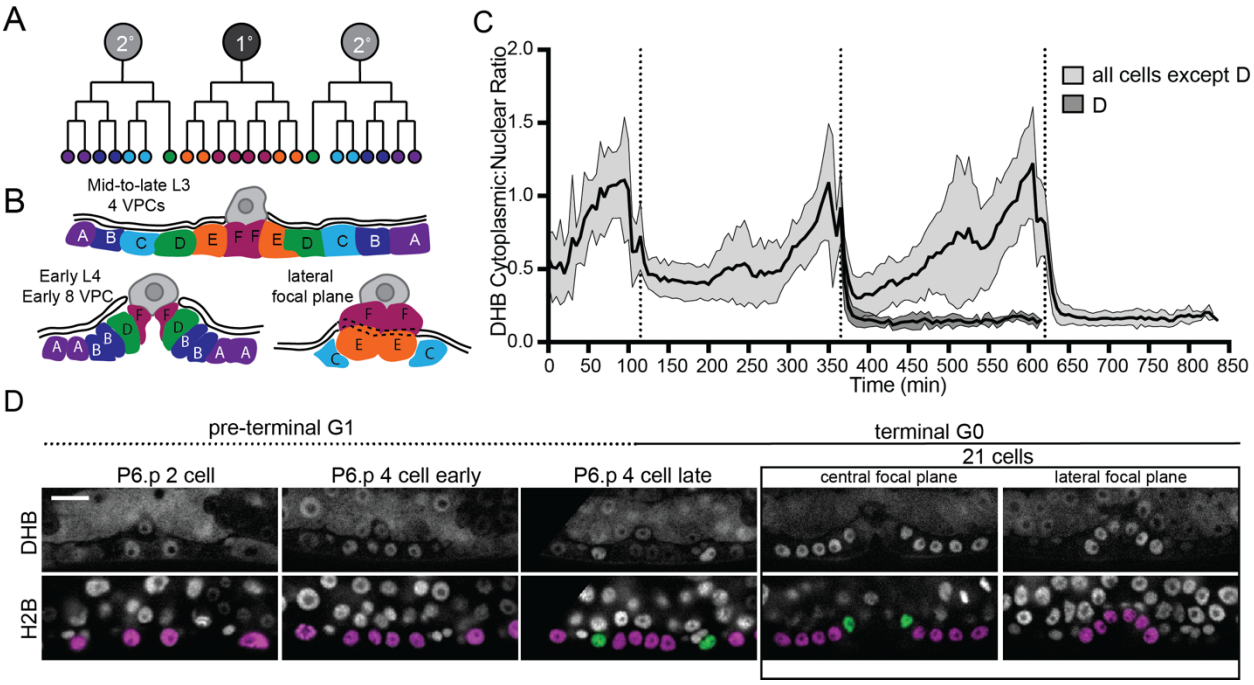

Figure 5. Vulval precursor cells exit terminal divisions into a CDK^{low} state. (A) Schematic of primary (1°) and secondary (2°) fated vulval precursor cells (VPCs). (B) All of the VPCs, with the exception of the D cells, divide to facilitate vulval morphogenesis. (C) Time series of DHB biosensor localization in the 1° and 2° VPCs over time, as measured every 5 minutes. Note that the terminally differentiated D cells are born into a CDK^{low} state ($n \geq 9$). (D) Representative images of DHB biosensor localization in the VPCs from the P6.p 2-cell stage to 8-cell stage. Nuclei (H2B) are highlighted in magenta for non-D cell 1° and 2° VPCs and green for the D cells. Scale bar = 10 μm. Dotted line indicates time of anaphase. Shaded error bands depict mean ± standard deviation.

Figure 6

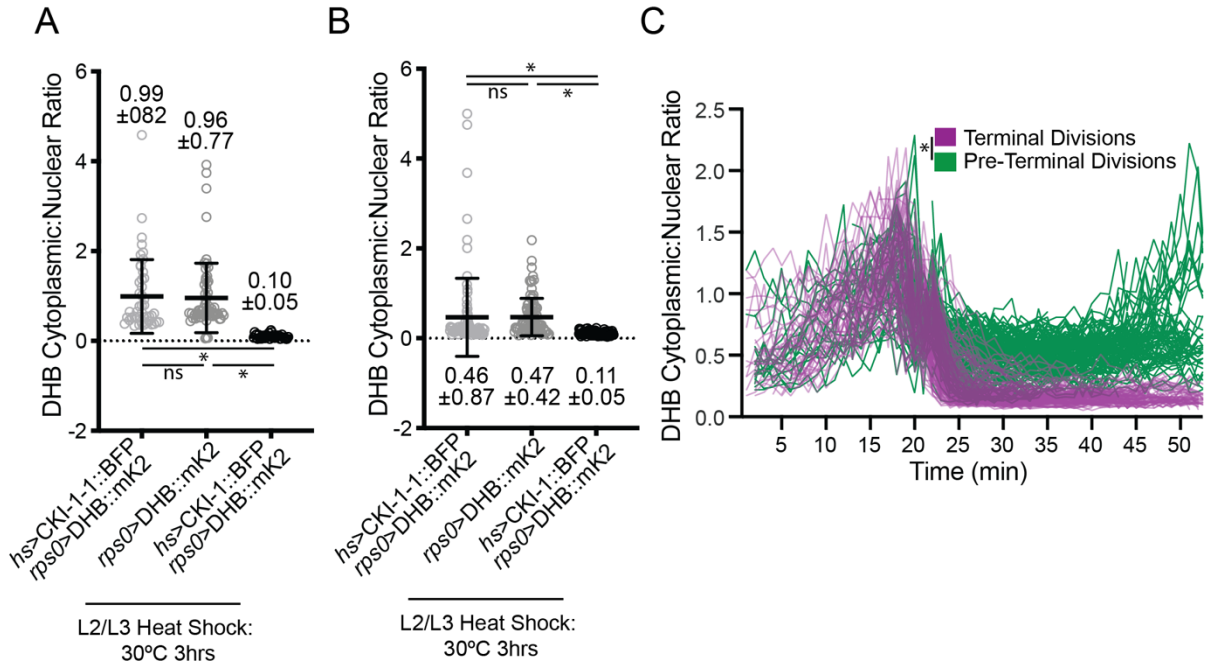

Figure 6. Induced G_0 arrest and terminal differentiation are both characterized by a CDK^{low} state. (A-B) Quantification of DHB biosensor localization in sex myoblast (SM) cells (A; ns P = 0.41085, *$P \leq 1x10^{-7}$) and vulval precursor cells (VPCs, B; ns P = 0.47997, *$P \leq 1x10^{-7}$) following ectopic expression of CKI-1 (*hsp*>CKI-1::2x-BFP) compared to non-heat shock controls and heat-shock animals without the transgene ($n \geq 36$ per treatment). (C) Time series of DHB biosensor localization in SM, VPCs, and SS/VU cells, comparing cycling cells (green) to terminally differentiated cells (magenta) ($n \geq 109$; *$P \leq 1x10^{-7}$). Error bars and shaded error bands depict mean ± standard deviation.

REFERENCES

Abe, T., Sakaue-Sawano, A., Kiyonari, H., Shioi, G., Inoue, K., Horiuchi, T., Nakao, K., Miyawaki, A., Aizawa, S., and Fujimori, T. (2013). Visualization of cell cycle in mouse embryos with Fucci2 reporter directed by Rosa26 promoter. Development *140*, 237-246.

Albert Hubbard, E.J., and Schedl, T. (2019). Biology of the Caenorhabditis elegans Germline Stem Cell System. Genetics *213*, 1145-1188.

Arora, M., Moser, J., Phadke, H., Basha, A.A., and Spencer, S.L. (2017). Endogenous Replication Stress in Mother Cells Leads to Quiescence of Daughter Cells. Cell Rep *19*, 1351-1364.

Artimo, P., Jonnalagedda, M., Arnold, K., Baratin, D., Csardi, G., de Castro, E., Duvaud, S., Flegel, V., Fortier, A., Gasteiger, E.*, et al.* (2012). ExPASy: SIB bioinformatics resource portal. Nucleic Acids Res *40*, W597-603.

Bajar, B.T., Lam, A.J., Badiee, R.K., Oh, Y.H., Chu, J., Zhou, X.X., Kim, N., Kim, B.B., Chung, M., Yablonovitch, A.L.*, et al.* (2016). Fluorescent indicators for simultaneous reporting of all four cell cycle phases. Nat Methods *13*, 993-996.

Bao, Z., Zhao, Z., Boyle, T.J., Murray, J.I., and Waterston, R.H. (2008). Control of cell cycle timing during C. elegans embryogenesis. Dev Biol *318*, 65-72.

Barnes, W.M. (1994). PCR amplification of up to 35-kb DNA with high fidelity and high yield from lambda bacteriophage templates. Proc Natl Acad Sci U S A *91*, 2216-2220.

Bosch, J.A., Colbeth, R., Zirin, J., and Perrimon, N. (2019). Gene Knock-Ins in Drosophila Using Homology-Independent Insertion of Universal Donor Plasmids. Genetics.

Bouldin, C.M., and Kimelman, D. (2014a). Cdc25 and the importance of G2 control: insights from developmental biology. Cell Cycle *13*, 2165-2171.

Bouldin, C.M., and Kimelman, D. (2014b). Dual fucci: a new transgenic line for studying the cell cycle from embryos to adults. Zebrafish *11*, 182-183.

Bouldin, C.M., Snelson, C.D., Farr, G.H., 3rd, and Kimelman, D. (2014). Restricted expression of cdc25a in the tailbud is essential for formation of the zebrafish posterior body. Genes Dev *28*, 384-395.

Brenner, S. (1974). The genetics of Caenorhabditis elegans. Genetics *77*, 71-94.

Buttitta, L.A., and Edgar, B.A. (2007). Mechanisms controlling cell cycle exit upon terminal differentiation. Curr Opin Cell Biol *19*, 697-704.

Buttitta, L.A., Katzaroff, A.J., and Edgar, B.A. (2010). A robust cell cycle control mechanism limits E2F-induced proliferation of terminally differentiated cells in vivo. J Cell Biol *189*, 981-996.

Buttitta, L.A., Katzaroff, A.J., Perez, C.L., de la Cruz, A., and Edgar, B.A. (2007). A double-assurance mechanism controls cell cycle exit upon terminal differentiation in Drosophila. Dev Cell *12*, 631-643.

Cappell, S.D., Chung, M., Jaimovich, A., Spencer, S.L., and Meyer, T. (2016). Irreversible APC(Cdh1) Inactivation Underlies the Point of No Return for Cell-Cycle Entry. Cell *166*, 167-180.

Celniker, S.E., Dillon, L.A., Gerstein, M.B., Gunsalus, K.C., Henikoff, S., Karpen, G.H., Kellis, M., Lai, E.C., Lieb, J.D., MacAlpine, D.M.*, et al.* (2009). Unlocking the secrets of the genome. Nature *459*, 927-930.

Chen, B.C., Legant, W.R., Wang, K., Shao, L., Milkie, D.E., Davidson, M.W., Janetopoulos, C., Wu, X.S., Hammer, J.A., 3rd, Liu, Z.*, et al.* (2014). Lattice light-sheet microscopy: imaging molecules to embryos at high spatiotemporal resolution. Science *346*, 1257998.

Clayton, J.E., van den Heuvel, S.J., and Saito, R.M. (2008). Transcriptional control of cell-cycle quiescence during C. elegans development. Dev Biol *313*, 603-613.

Cohen-Fix, O., and Askjaer, P. (2017). Cell Biology of the Caenorhabditis elegans Nucleus. Genetics *205*, 25-59.

Cranfill, P.J., Sell, B.R., Baird, M.A., Allen, J.R., Lavagnino, Z., de Gruiter, H.M., Kremers, G.J., Davidson, M.W., Ustione, A., and Piston, D.W. (2016). Quantitative assessment of fluorescent proteins. Nat Methods *13*, 557-562.

de la Cova, C., Townley, R., Regot, S., and Greenwald, I. (2017). A Real-Time Biosensor for ERK Activity Reveals Signaling Dynamics during C. elegans Cell Fate Specification. Dev Cell *42*, 542-553 e544.

Dickinson, D.J., Pani, A.M., Heppert, J.K., Higgins, C.D., and Goldstein, B. (2015). Streamlined Genome Engineering with a Self-Excising Drug Selection Cassette. Genetics.

Dickinson, D.J., Ward, J.D., Reiner, D.J., and Goldstein, B. (2013). Engineering the Caenorhabditis elegans genome using Cas9-triggered homologous recombination. Nat Methods *10*, 1028-1034.

Du, Z., Santella, A., He, F., Shah, P.K., Kamikawa, Y., and Bao, Z. (2015). The Regulatory Landscape of Lineage Differentiation in a Metazoan Embryo. Dev Cell *34*, 592-607.

Dwivedi, V.K., Pardo-Pastor, C., Droste, R., Denning, D.P., Rosenblatt, J., and Horvitz, H.R. (2019). Cell cycle S-phase arrest drives cell extrusion. bioRxiv, 839845.

Edgar, L.G., and McGhee, J.D. (1988). DNA synthesis and the control of embryonic gene expression in C. elegans. Cell *53*, 589-599.

Elinson, R.P. (2011). Cleavage and Gastrulation in Xenopus laevis Embryos. In eLS.

Esteves de Lima, J., Bonnin, M.A., Bourgeois, A., Parisi, A., Le Grand, F., and Duprez, D. (2014). Specific pattern of cell cycle during limb fetal myogenesis. Dev Biol *392*, 308-323.

Farrell, J.A., and O'Farrell, P.H. (2014). From egg to gastrula: how the cell cycle is remodeled during the Drosophila mid-blastula transition. Annu Rev Genet *48*, 269-294.

Fire, A., Xu, S., Montgomery, M.K., Kostas, S.A., Driver, S.E., and Mello, C.C. (1998). Potent and specific genetic interference by double-stranded RNA in Caenorhabditis elegans. Nature *391*, 806-811.

Foe, V.E. (1989). Mitotic domains reveal early commitment of cells in Drosophila embryos. Development *107*, 1-22.

Ford, M.J., Yeyati, P.L., Mali, G.R., Keighren, M.A., Waddell, S.H., Mjoseng, H.K., Douglas, A.T., Hall, E.A., Sakaue-Sawano, A., Miyawaki, A.*, et al.* (2018). A Cell/Cilia Cycle Biosensor for Single-Cell Kinetics Reveals Persistence of Cilia after G1/S Transition Is a General Property in Cells and Mice. Dev Cell *47*, 509-523 e505.

Fox, P.M., Vought, V.E., Hanazawa, M., Lee, M.H., Maine, E.M., and Schedl, T. (2011). Cyclin E and CDK-2 regulate proliferative cell fate and cell cycle progression in the C. elegans germline. Development *138*, 2223-2234.

Fukuhara, S., Zhang, J., Yuge, S., Ando, K., Wakayama, Y., Sakaue-Sawano, A., Miyawaki, A., and Mochizuki, N. (2014). Visualizing the cell-cycle progression of endothelial cells in zebrafish. Dev Biol *393*, 10-23.

Gao, L., Shao, L., Chen, B.C., and Betzig, E. (2014). 3D live fluorescence imaging of cellular dynamics using Bessel beam plane illumination microscopy. Nat Protoc *9*, 1083-1101.

Gast, C.E., Silk, A.D., Zarour, L., Riegler, L., Burkhart, J.G., Gustafson, K.T., Parappilly, M.S., Roh-Johnson, M., Goodman, J.R., Olson, B.*, et al.* (2018). Cell fusion potentiates tumor heterogeneity and reveals circulating hybrid cells that correlate with stage and survival. Sci Adv *4*, eaat7828.

Gibson, D.G., Smith, H.O., Hutchison, C.A., 3rd, Venter, J.C., and Merryman, C. (2010). Chemical synthesis of the mouse mitochondrial genome. Nat Methods *7*, 901-903.

Gibson, D.G., Young, L., Chuang, R.Y., Venter, J.C., Hutchison, C.A., 3rd, and Smith, H.O. (2009). Enzymatic assembly of DNA molecules up to several hundred kilobases. Nat Methods *6*, 343-345.

Gookin, S., Min, M., Phadke, H., Chung, M., Moser, J., Miller, I., Carter, D., and Spencer, S.L. (2017). A map of protein dynamics during cell-cycle progression and cell-cycle exit. PLoS Biol *15*, e2003268.

Grant, G.D., Kedziora, K.M., Limas, J.C., Purvis, J.E., and Cook, J.G. (2018). Precise detection of S phase onset reveals decoupled G1/S transition events. bioRxiv, 300442.

Grosshans, J., and Wieschaus, E. (2000). A genetic link between morphogenesis and cell division during formation of the ventral furrow in Drosophila. Cell *101*, 523-531.

Haeckel, E.H.P.A. (1903). Anthropogenie, oder, Entwickelungsgeschichte des Menschen: Keimes- und Stammes-Geschichte (Leipzig: W. Englemann).

Hahn, A.T., Jones, J.T., and Meyer, T. (2009). Quantitative analysis of cell cycle phase durations and PC12 differentiation using fluorescent biosensors. Cell Cycle *8*, 1044-1052.

Hanahan, D., and Weinberg, R.A. (2011). Hallmarks of cancer: the next generation. Cell *144*, 646-674.

Harris, T.W., Arnaboldi, V., Cain, S., Chan, J., Chen, W.J., Cho, J., Davis, P., Gao, S., Grove, C.A., Kishore, R.*, et al.* (2019). WormBase: a modern Model Organism Information Resource. Nucleic Acids Res.

Heppert, J.K., Dickinson, D.J., Pani, A.M., Higgins, C.D., Steward, A., Ahringer, J., Kuhn, J.R., and Goldstein, B. (2016). Comparative assessment of fluorescent proteins for in vivo imaging in an animal model system. Mol Biol Cell.

Hertzler, P.L., and Clark, W.H., Jr. (1992). Cleavage and gastrulation in the shrimp Sicyonia ingentis: invagination is accompanied by oriented cell division. Development *116*, 127-140.

Hong, Y., Roy, R., and Ambros, V. (1998). Developmental regulation of a cyclin-dependent kinase inhibitor controls postembryonic cell cycle progression in Caenorhabditis elegans. Development *125*, 3585-3597.

Inoue, S. (1953). Polarization optical studies of the mitotic spindle. I. The demonstration of spindle fibers in living cells. Chromosoma *Bd. 5*, 33.

Jukam, D., Shariati, S.A.M., and Skotheim, J.M. (2017). Zygotic Genome Activation in Vertebrates. Dev Cell *42*, 316-332.

Kagawa, Y., Matsumoto, S., Kamioka, Y., Mimori, K., Naito, Y., Ishii, T., Okuzaki, D., Nishida, N., Maeda, S., Naito, A.*, et al.* (2013). Cell cycle-dependent Rho GTPase activity dynamically regulates cancer cell motility and invasion in vivo. PLoS One *8*, e83629.

Katz, W.S., Hill, R.J., Clandinin, T.R., and Sternberg, P.W. (1995). Different levels of the C. elegans growth factor LIN-3 promote distinct vulval precursor fates. Cell *82*, 297-307.

Kelley, L.C., Wang, Z., Hagedorn, E.J., Wang, L., Shen, W., Lei, S., Johnson, S.A., and Sherwood, D.R. (2017). Live-cell confocal microscopy and quantitative 4D image analysis of anchor-cell invasion through the basement membrane in Caenorhabditis elegans. Nat Protoc *12*, 2081-2096.

Kimble, J., and Hirsh, D. (1979). The Postembryonic Cell Lineages of the Hermaphrodite and Male Gonads in *Caenorhabditis elegans*. Dev Biol *70*, 396-417.

Kirby, C., Kusch, M., and Kemphues, K. (1990). Mutations in the par genes of Caenorhabditis elegans affect cytoplasmic reorganization during the first cell cycle. Dev Biol *142*, 203-215.

Kocsisova, Z., Kornfeld, K., and Schedl, T. (2018). Cell cycle accumulation of the proliferating cell nuclear antigen PCN-1 transitions from continuous in the adult germline to intermittent in the early embryo of C. elegans. BMC Dev Biol *18*, 12.

Koh, S.B., Mascalchi, P., Rodriguez, E., Lin, Y., Jodrell, D.I., Richards, F.M., and Lyons, S.K. (2017). A quantitative FastFUCCI assay defines cell cycle dynamics at a single-cell level. J Cell Sci *130*, 512-520.

Kohrman, A.Q., and Matus, D.Q. (2017). Divide or Conquer: Cell Cycle Regulation of Invasive Behavior. Trends Cell Biol *27*, 12-25.

Korzelius, J., The, I., Ruijtenberg, S., Prinsen, M.B., Portegijs, V., Middelkoop, T.C., Groot Koerkamp, M.J., Holstege, F.C., Boxem, M., and van den Heuvel, S. (2011). Caenorhabditis elegans cyclin D/CDK4 and cyclin E/CDK2 induce distinct cell cycle re-entry programs in differentiated muscle cells. PLoS Genet *7*, e1002362.

Kudo, T., Jeknic, S., Macklin, D.N., Akhter, S., Hughey, J.J., Regot, S., and Covert, M.W. (2018). Live-cell measurements of kinase activity in single cells using translocation reporters. Nat Protoc *13*, 155-169.

Kuriya, K., Higashiyama, E., Avsar-Ban, E., Okochi, N., Hattori, K., Ogata, S., Takebayashi, S., Ogata, M., Tamaru, Y., and Okumura, K. (2016). Direct visualization of replication dynamics in early zebrafish embryos. Biosci Biotechnol Biochem *80*, 945-948.

Kurth, T. (2005). A cell cycle arrest is necessary for bottle cell formation in the early Xenopus gastrula: integrating cell shape change, local mitotic control and mesodermal patterning. Mech Dev *122*, 1251-1265.

Lahl, V., Halama, C., and Schierenberg, E. (2003). Comparative and experimental embryogenesis of Plectidae (Nematoda). Dev Genes Evol *213*, 18-27.

Langley, A.R., Smith, J.C., Stemple, D.L., and Harvey, S.A. (2014). New insights into the maternal to zygotic transition. Development *141*, 3834-3841.

Liu, T.L., Upadhyayula, S., Milkie, D.E., Singh, V., Wang, K., Swinburne, I.A., Mosaliganti, K.R., Collins, Z.M., Hiscock, T.W., Shea, J.*, et al.* (2018). Observing the cell in its native state: Imaging subcellular dynamics in multicellular organisms. Science *360*.

Ma, Y., McKay, D.J., and Buttitta, L. (2019). Changes in chromatin accessibility ensure robust cell cycle exit in terminally differentiated cells. PLoS Biol *17*, e3000378.

Mac Auley, A., Werb, Z., and Mirkes, P.E. (1993). Characterization of the unusually rapid cell cycles during rat gastrulation. Development *117*, 873-883.

Maddox, A.S., and Maddox, P.S. (2012). High-resolution imaging of cellular processes in Caenorhabditis elegans. Methods Cell Biol *107*, 1-34.

Matus, D.Q., Chang, E., Makohon-Moore, S.C., Hagedorn, M.A., Chi, Q.Y., and Sherwood, D.R. (2014). Cell division and targeted cell cycle arrest opens and stabilizes basement membrane gaps. Nature Communications *5*, 13.

Matus, D.Q., Lohmer, L.L., Kelley, L.C., Schindler, A.J., Kohrman, A.Q., Barkoulas, M., Zhang, W., Chi, Q., and Sherwood, D.R. (2015). Invasive Cell Fate Requires G1 Cell-Cycle Arrest and Histone Deacetylase-Mediated Changes in Gene Expression. Developmental Cell *35*, 162-174.

Medwig-Kinney, T.N., Smith, J.J., Palmisano, N.J., Tank, S., Zhang, W., and Matus, D.Q. (2019). A developmental gene regulatory network for C. elegans anchor cell invasion. Development.

Miller, I., Min, M., Yang, C., Tian, C., Gookin, S., Carter, D., and Spencer, S.L. (2018). Ki67 is a Graded Rather than a Binary Marker of Proliferation versus Quiescence. Cell Rep *24*, 1105-1112 e1105.

Miwa, S., Yano, S., Kimura, H., Yamamoto, M., Toneri, M., Matsumoto, Y., Uehara, F., Hiroshima, Y., Murakami, T., Hayashi, K.*, et al.* (2015). Cell-cycle fate-monitoring distinguishes individual chemosensitive and chemoresistant cancer cells in drug-treated heterogeneous populations demonstrated by real-time FUCCI imaging. Cell Cycle *14*, 621-629.

Mort, R.L., Ford, M.J., Sakaue-Sawano, A., Lindstrom, N.O., Casadio, A., Douglas, A.T., Keighren, M.A., Hohenstein, P., Miyawaki, A., and Jackson, I.J. (2014). Fucci2a: a bicistronic cell cycle reporter that allows Cre mediated tissue specific expression in mice. Cell Cycle *13*, 2681-2696.

Moser, J., Miller, I., Carter, D., and Spencer, S.L. (2018). Control of the Restriction Point by Rb and p21. Proc Natl Acad Sci U S A *115*, E8219-E8227.

Murakami, M.S., Moody, S.A., Daar, I.O., and Morrison, D.K. (2004). Morphogenesis during Xenopus gastrulation requires Wee1-mediated inhibition of cell proliferation. Development *131*, 571-580.

Ogura, Y., Sakaue-Sawano, A., Nakagawa, M., Satoh, N., Miyawaki, A., and Sasakura, Y. (2011). Coordination of mitosis and morphogenesis: role of a prolonged G2 phase during chordate neurulation. Development *138*, 577-587.

Oki, T., Nishimura, K., Kitaura, J., Togami, K., Maehara, A., Izawa, K., Sakaue-Sawano, A., Niida, A., Miyano, S., Aburatani, H.*, et al.* (2014). A novel cell-cycle-indicator, mVenus-p27K-, identifies quiescent cells and visualizes G0-G1 transition. Sci Rep *4*, 4012.

Overton, K.W., Spencer, S.L., Noderer, W.L., Meyer, T., and Wang, C.L. (2014). Basal p21 controls population heterogeneity in cycling and quiescent cell cycle states. Proc Natl Acad Sci U S A *111*, E4386-4393.

Ozpolat, B.D., Handberg-Thorsager, M., Vervoort, M., and Balavoine, G. (2017). Cell lineage and cell cycling analyses of the 4d micromere using live imaging in the marine annelid Platynereis dumerilii. Elife *6*.

Pai, V.P., Lemire, J.M., Pare, J.F., Lin, G., Chen, Y., and Levin, M. (2015). Endogenous gradients of resting potential instructively pattern embryonic neural tissue via Notch signaling and regulation of proliferation. J Neurosci *35*, 4366-4385.

Paix, A., Folkmann, A., Rasoloson, D., and Seydoux, G. (2015). High Efficiency, Homology-Directed Genome Editing in Caenorhabditis elegans Using CRISPR-Cas9 Ribonucleoprotein Complexes. Genetics *201*, 47-54.

Paix, A., Wang, Y., Smith, H., Lee, C.Y., Calidas, D., Lu, T., Smith, J., Schmidt, H., Krause, M., and Seydoux, G. (2014). Scalable and Versatile Genome Editing Using Linear DNAs with Micro-homology to Cas9 Sites in Caenorhabditis elegans. Genetics.

Perry, K.J., and Henry, J.Q. (2015). CRISPR/Cas9-mediated genome modification in the mollusc, Crepidula fornicata. Genesis *53*, 237-244.

Pineda, G., Lennon, K.M., Delos Santos, N.P., Lambert-Fliszar, F., Riso, G.L., Lazzari, E., Marra, M.A., Morris, S., Sakaue-Sawano, A., Miyawaki, A.*, et al.* (2016). Tracking of Normal and Malignant Progenitor Cell Cycle Transit in a Defined Niche. Sci Rep *6*, 23885.

Rasmussen, J.P., Feldman, J.L., Reddy, S.S., and Priess, J.R. (2013). Cell interactions and patterned intercalations shape and link epithelial tubes in C. elegans. PLoS Genet *9*, e1003772.

Redemann, S., Schloissnig, S., Ernst, S., Pozniakowsky, A., Ayloo, S., Hyman, A.A., and Bringmann, H. (2011). Codon adaptation-based control of protein expression in C. elegans. Nat Methods *8*, 250-252.

Regot, S., Hughey, J.J., Bajar, B.T., Carrasco, S., and Covert, M.W. (2014). High-sensitivity measurements of multiple kinase activities in live single cells. Cell *157*, 1724-1734.

Ridenour, D.A., McKinney, M.C., Bailey, C.M., and Kulesa, P.M. (2012). CycleTrak: a novel system for the semi-automated analysis of cell cycle dynamics. Dev Biol *365*, 189-195.

Ross, B.L., Tenner, B., Markwardt, M.L., Zviman, A., Shi, G., Kerr, J.P., Snell, N.E., McFarland, J.J., Mauban, J.R., Ward, C.W.*, et al.* (2018). Single-color, ratiometric biosensors for detecting signaling activities in live cells. Elife *7*.

Rual, J.F., Ceron, J., Koreth, J., Hao, T., Nicot, A.S., Hirozane-Kishikawa, T., Vandenhaute, J., Orkin, S.H., Hill, D.E., van den Heuvel, S.*, et al.* (2004). Toward improving Caenorhabditis elegans phenome mapping with an ORFeome-based RNAi library. Genome Res *14*, 2162-2168.

Ruijtenberg, S., and van den Heuvel, S. (2015). G1/S Inhibitors and the SWI/SNF Complex Control Cell-Cycle Exit during Muscle Differentiation. Cell.

Saito, R.M., Perreault, A., Peach, B., Satterlee, J.S., and van den Heuvel, S. (2004). The CDC-14 phosphatase controls developmental cell-cycle arrest in C. elegans. Nature Cell Biology *6*, 777-783.

Sakaue-Sawano, A., Kurokawa, H., Morimura, T., Hanyu, A., Hama, H., Osawa, H., Kashiwagi, S., Fukami, K., Miyata, T., Miyoshi, H.*, et al.* (2008). Visualizing Spatiotemporal Dynamics of Multicellular Cell-Cycle Progression. Cell *132*, 487-498.

Sakaue-Sawano, A., Yo, M., Komatsu, N., Hiratsuka, T., Kogure, T., Hoshida, T., Goshima, N., Matsuda, M., Miyoshi, H., and Miyawaki, A. (2017). Genetically Encoded Tools for Optical Dissection of the Mammalian Cell Cycle. Mol Cell *68*, 626-640 e625.

Salic, A., and Mitchison, T.J. (2008). A chemical method for fast and sensitive detection of DNA synthesis in vivo. Proc Natl Acad Sci U S A *105*, 2415-2420.

Schindelin, J., Arganda-Carreras, I., Frise, E., Kaynig, V., Longair, M., Pietzsch, T., Preibisch, S., Rueden, C., Saalfeld, S., Schmid, B.*, et al.* (2012). Fiji: an open-source platform for biological-image analysis. Nat Methods *9*, 676-682.

Schwarz, C., Johnson, A., Koivomagi, M., Zatulovskiy, E., Kravitz, C.J., Doncic, A., and Skotheim, J.M. (2018). A Precise Cdk Activity Threshold Determines Passage through the Restriction Point. Mol Cell *69*, 253-264 e255.

Shemiakina, II, Ermakova, G.V., Cranfill, P.J., Baird, M.A., Evans, R.A., Souslova, E.A., Staroverov, D.B., Gorokhovatsky, A.Y., Putintseva, E.V., Gorodnicheva, T.V.*, et al.* (2012). A monomeric red fluorescent protein with low cytotoxicity. Nat Commun *3*, 1204.

Singh, A.M., Chappell, J., Trost, R., Lin, L., Wang, T., Tang, J., Matlock, B.K., Weller, K.P., Wu, H., Zhao, S.*, et al.* (2013). Cell-cycle control of developmentally regulated transcription factors accounts for heterogeneity in human pluripotent cells. Stem Cell Reports *1*, 532-544.

Singh, A.M., Sun, Y., Li, L., Zhang, W., Wu, T., Zhao, S., Qin, Z., and Dalton, S. (2015). Cell-Cycle Control of Bivalent Epigenetic Domains Regulates the Exit from Pluripotency. Stem Cell Reports *5*, 323-336.

Soufi, A., and Dalton, S. (2016). Cycling through developmental decisions: how cell cycle dynamics control pluripotency, differentiation and reprogramming. Development *143*, 4301-4311.

Spencer, S.L., Cappell, S.D., Tsai, F.C., Overton, K.W., Wang, C.L., and Meyer, T. (2013). The proliferation-quiescence decision is controlled by a bifurcation in CDK2 activity at mitotic exit. Cell *155*, 369-383.

Sternberg, P.W., and Horvitz, H.R. (1986). Pattern formation during vulval development in C. elegans. Cell *44*, 761-772.

Sternberg, S.R., and Corporation, C. (1983). Biomedical Image Processing. Computer *16*, 22-34.

Sugiyama, M., Sakaue-Sawano, A., Iimura, T., Fukami, K., Kitaguchi, T., Kawakami, K., Okamoto, H., Higashijima, S., and Miyawaki, A. (2009). Illuminating cell-cycle progression in the developing zebrafish embryo. Proc Natl Acad Sci U S A *106*, 20812-20817.

Sulston, J.E., and Horvitz, H.R. (1977). Post-embryonic cell lineages of the nematode, Caenorhabditis elegans. Dev Biol *56*, 110-156.

Timney, B.L., Raveh, B., Mironska, R., Trivedi, J.M., Kim, S.J., Russel, D., Wente, S.R., Sali, A., and Rout, M.P. (2016). Simple rules for passive diffusion through the nuclear pore complex. J Cell Biol *215*, 57-76.

van der Horst, S.E.M., Cravo, J., Woollard, A., Teapal, J., and van den Heuvel, S. (2019). C. elegans Runx/CBFbeta suppresses POP-1 TCF to convert asymmetric to proliferative division of stem cell-like seam cells. Development *146*.

van Rijnberk, L.M., van der Horst, S.E., van den Heuvel, S., and Ruijtenberg, S. (2017). A dual transcriptional reporter and CDK-activity sensor marks cell cycle entry and progression in C. elegans. PLoS One *12*, e0171600.

Wong, M.C., Martynovsky, M., and Schwarzbauer, J.E. (2011). Analysis of cell migration using Caenorhabditis elegans as a model system. Methods Mol Biol *769*, 233-247.

Wong, M.K., Guan, D., Ng, K.H., Ho, V.W., An, X., Li, R., Ren, X., and Zhao, Z. (2016). Timing of Tissue-specific Cell Division Requires a Differential Onset of Zygotic Transcription during Metazoan Embryogenesis. J Biol Chem *291*, 12501-12513.

Yang, R., and Feldman, J.L. (2015). SPD-2/CEP192 and CDK Are Limiting for Microtubule-Organizing Center Function at the Centrosome. Curr Biol *25*, 1924-1931.

Yang, Z.J., Broz, D.K., Noderer, W.L., Ferreira, J.P., Overton, K.W., Spencer, S.L., Meyer, T., Tapscott, S.J., Attardi, L.D., and Wang, C.L. (2015). p53 suppresses muscle differentiation at the myogenin step in response to genotoxic stress. Cell Death Differ *22*, 560-573.

Yano, S., Miwa, S., Mii, S., Hiroshima, Y., Uehara, F., Kishimoto, H., Tazawa, H., Zhao, M., Bouvet, M., Fujiwara, T.*, et al.* (2015). Cancer cells mimic in vivo spatial-temporal cell-cycle phase distribution and chemosensitivity in 3-dimensional Gelfoam(R) histoculture but not 2-dimensional culture as visualized with real-time FUCCI imaging. Cell Cycle *14*, 808-819.

Yano, S., Miwa, S., Mii, S., Hiroshima, Y., Uehara, F., Yamamoto, M., Kishimoto, H., Tazawa, H., Bouvet, M., Fujiwara, T.*, et al.* (2014a). Invading cancer cells are predominantly in G0/G1 resulting in chemoresistance demonstrated by real-time FUCCI imaging. Cell Cycle *13*, 953-960.

Yano, S., Zhang, Y., Miwa, S., Tome, Y., Hiroshima, Y., Uehara, F., Yamamoto, M., Suetsugu, A., Kishimoto, H., Tazawa, H.*, et al.* (2014b). Spatial-temporal FUCCI imaging of each cell in a tumor demonstrates locational dependence of cell cycle dynamics and chemoresponsiveness. Cell Cycle *13*, 2110-2119.

Ziel, J.W., Hagedorn, E.J., Audhya, A., and Sherwood, D.R. (2009). UNC-6 (netrin) orients the invasive membrane of the anchor cell in C. elegans. Nature Cell Biology *11*, 183-189.

Zielke, N., and Edgar, B.A. (2015). FUCCI sensors: powerful new tools for analysis of cell proliferation. Wiley Interdiscip Rev Dev Biol *4*, 469-487.

Zielke, N., Korzelius, J., van Straaten, M., Bender, K., Schuhknecht, G.F.P., Dutta, D., Xiang, J., and Edgar, B.A. (2014). Fly-FUCCI: A versatile tool for studying cell proliferation in complex tissues. Cell Rep *7*, 588-598.

Zielke, N., van Straaten, M., Bohlen, J., and Edgar, B.A. (2016). Using the Fly-FUCCI System for the Live Analysis of Cell Cycle Dynamics in Cultured Drosophila Cells. Methods Mol Biol *1342*, 305-320.